When de Prony Met Leonardo: An Automatic Algorithm for Chemical Element Extraction From Macro X-Ray Fluorescence Data

Su Yan, *Student Member, IEEE*, Jun-Jie Huang, *Member, IEEE*, Nathan Daly, Catherine Higgitt, and Pier Luigi Dragotti, *Fellow, IEEE*

***Abstract*—Macro X-ray Fluorescence (MA-XRF) scanning is an increasingly widely used technique for analytical imaging of paintings and other artworks. The datasets acquired must be processed to produce maps showing the distribution of the chemical elements that are present in the painting. Existing approaches require varying degrees of expert user intervention, in particular to select a list of target elements against which to fit the data. In this paper, we propose a novel approach that can automatically extract and identify chemical elements and their distributions from MA-XRF datasets. The proposed approach consists of three parts: 1) pre-processing steps, 2) pulse detection and model order selection based on Finite Rate of Innovation theory, and 3) chemical element estimation based on Cramér-Rao bounding techniques. The performance of our approach is assessed using MA-XRF datasets acquired from paintings in the collection of the National Gallery, London. The results presented show the ability of our approach to detect elements with weak X-ray fluorescence intensity and from noisy XRF spectra, to separate overlapping elemental signals and, excitingly, to aid visualisation of hidden underdrawing in a masterpiece by Leonardo da Vinci.**

***Index Terms*—Macro X-ray Fluorescence scanning, XRF deconvolution, finite rate of innovation, historical paintings, estimation and detection.**

I. Introduction

EASEL painting has been one of the most influential and important forms of art since the 13th century. To avoid invasive procedures such as sample removal, various non-destructive analytical imaging techniques are increasingly being used to investigate paintings and obtain valuable information about their composition, creation, history, and to inform their future preservation. For this reason, there is a growing interest in developing new image and signal processing methods to process the large and often multimodal datasets produced using these new analytical imaging methods (see for example [2]–[7]).

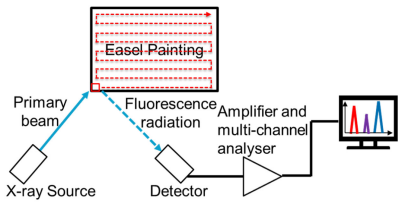

Fig. 1. Schematic of the acquisition of an MA-XRF dataset from an easel painting.

Macro X-ray fluorescence (MA-XRF) scanning is a technique that can be used for non-invasive elemental analysis of paintings. Since different pigments used in the painting may contain different elements, producing the distribution maps of the elements can give further information about an artist's palette, improve the understanding of their painting techniques, for example by revealing how paint layers have been built up, and even reveal hidden features of the painting. Fig. 1 shows the schematic working of an MA-XRF scanning device. The X-ray source illuminates sub-millimetre spots of a painting with a primary X-ray beam, leading to electronic transitions and exciting the emission of characteristic X-ray photons from the atoms of chemical elements that are present in the painting. The energy of the released photons (E_c) is equal to the energy difference between the two shells where the electronic transition occurs, which is characteristic of the atom of a chemical element. The detector, with its amplifier and multi-channel analyser, then collects and counts the released X-ray photons with respect to their energy levels, resulting in a pixel of data in the form of a spectrum. Due to the effect of the detector, the spectral response for each characteristic element X-ray (also called an element line) is in the form of a narrow Gaussian-shaped peak (covering a range of energies) [8]–[10], hereafter called a pulse. As a result, the observed XRF spectrum can be regarded as a combination of several Gaussian pulses, as shown in Fig. 2. This broadened pulse shape leads to a problem that the pulses of nearby characteristic X-rays overlap. The task of separating the overlapping pulses and identifying the elements present and their net intensities from the XRF spectrum is called XRF spectrum *deconvolution*. Since a painting is created using complex pigment mixtures and

Manuscript received January 22, 2021; revised June 21, 2021; accepted July 27, 2021. Date of publication August 10, 2021; date of current version September 2, 2021. This work was supported by EPSRC under Grant EP/R032785/1. The work of Su Yan was supported by China Scholarship Council (CSC) Scholarship. This work was presented at ICASSP 2020 [1]. *(Corresponding author: Jun-Jie Huang.)*

Su Yan, Jun-Jie Huang, and Pier Luigi Dragotti are with the Electrical and Electronic Engineering, Imperial College London, London SW7 2AZ, U.K. (e-mail: s.yan18@imperial.ac.uk; j.huang15@imperial.ac.uk; p.dragotti@imperial.ac.uk).

Nathan Daly and Catherine Higgitt are with the Scientific Department, The National Gallery, London WC2N 5DN, U.K. (e-mail: nathan.daly@ng-london.org.uk; catherine.higgitt@ng-london.org.uk).

This article has supplementary downloadable material available at https://doi.org/10.1109/TCI.2021.3102820, provided by the authors.

Digital Object Identifier 10.1109/TCI.2021.3102820

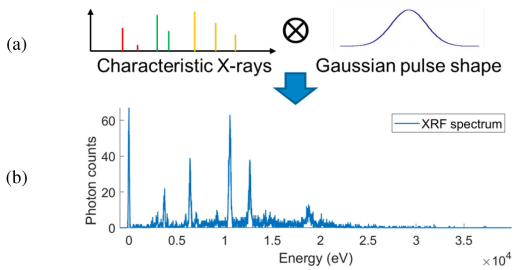

Fig. 2. The observed XRF spectrum of a single pixel of the MA-XRF datacube. The painting was scanned with a Bruker M6 JETSTREAM instrument.

layers, many elements are excited and detected at a single spot, making it challenging to deconvolve the spectrum.

Many approaches have been proposed for XRF spectrum deconvolution, based on the use of linear or nonlinear regressions or Bayesian methods to fit the XRF spectrum with Gaussian functions [8], of which those most relevant to MA-XRF scanning are described here. Van Espen *et al.* [11]–[13] created 'AXIL' (Analysis of X-ray spectra by Iterative least Squares), which fits the element pulses with Gaussian functions and the background with a polynomial using iterative least-squares. Developing from this, Solé *et al.* [14] created an open source software named 'PyMca', which similarly fits the XRF spectrum with Gaussian functions using non-linear least-squares but also takes specific characteristic lines as well as layered samples into consideration. Alfeld and Janssens [15] developed 'Datamuncher' in Interactive Data Language (IDL) for fast processing of the huge datasets typically produced with MA-XRF scanning and to produce artefact-free elemental distribution maps (from one or more datasets), by making use of the fitting with AXIL or PyMca and Dynamic Analysis (DA) [16], [17]. These tools were used by the original developers of the now commercially available M6 JETSTREAM MA-XRF scanning instrument produced by Bruker Corporation, the instrument most widely adopted for use by the heritage sector [18]. Conover proposed a method that uses non-linear regression to fit the XRF spectrum with Gaussian functions centred at the element characteristic energies [19]. However, this method relies on XRF spectra with high signal-to-noise ratios which require long acquisition time. Most instrument producers also provide proprietary deconvolution and quantification tools in the software for their instruments, including Bruker Corporation for their M6 JETSTREAM, although these packages have not necessarily been developed for MA-XRF scanning specifically.

Fitting XRF spectra with Gaussian functions requires knowledge of the number, widths and locations of the Gaussian functions. The widths can be obtained by measurement [19] or existing models [11], [15]. However, the number and locations of the Gaussian functions are unknown parameters related to the chemical elements present in the painting, where the number should be the total number of characteristic X-rays for these elements and the locations should be the energies of the characteristic X-rays. As a result, all existing approaches require user input to determine which element are likely to be present in the dataset. These approaches then fit the spectra based on the specified elements and indicate their distributions in the painting. However, the resulting element distribution maps from a given dataset can sometimes be completely different if the precise selection of elements changes (e.g. elements missed or added in error), making the results inconsistent. As a result, the selection of elements by the user has a significant effect on the accuracy of the final results.

In this paper, we propose a novel approach to automatically produce the element distribution maps from MA-XRF datasets. Our method does not require users to build a complex model or to input any predictions of elements present in the painting, making it much easier and more friendly to use. The proposed approach has been deliberately designed to assist in the detection of very weak element signals and can be divided into the following parts. Firstly, some pre-processing steps are implemented to estimate the shapes of the characteristic X-ray pulses in the XRF spectra. Then, the elemental pulses in the XRF spectra are localised and detected using variations of Finite Rate of Innovation (FRI) theory [20], [21] and Prony's method [22]. In this context we also propose an approach to estimate the number of pulses in a spectrum. After that, the detected pulses are assigned to the appropriate characteristic element X-rays to identify which chemical elements are present in each pixel of the painting. Finally, two distribution maps, a confidence map and a quantity map, are produced for each line group of each detected element. The assignment of the pulses to the elements and the confidence maps are obtained by leveraging Cramér-Rao bounding techniques [23]. The performance of our proposed approach is assessed using MA-XRF datasets acquired from paintings in the collection of the National Gallery, London, and the elemental maps produced by our algorithm are compared with those produced using the Bruker M6 software. The results demonstrate the ability of our method to automatically handle datasets with overlapping pulses, even when the datasets are noisy as is commonly the case with MA-XRF scanning of easel paintings. More importantly, our algorithm is able to detect weak signals in such datasets and was thus able to reveal the hidden underdrawings in three regions of the painting 'The Virgin of the Rocks' by Leonardo da Vinci without any additional user intervention.

II. Background

In this section, we first review some important properties of XRF spectra and MA-XRF datasets acquired from easel paintings. In this way we can also highlight challenges encountered when analysing this type of data.

A. Characteristic X-rays

Each chemical element has a unique atomic structure and atomic energy levels, and thus for each element, transitions between different electronic shells (or sub-shells) release photons with a unique set of energies, called characteristic X-rays [24]. The characteristic X-rays of an element are generated in series (e.g. K-series, L-series, M-series, etc.) and in this paper we consider 11 dominant characteristic X-rays, including $K_{\alpha 1}$, $K_{\alpha 2}$, $K_{\beta 1}$, $K_{\beta 2}$, L_l, $L_{\alpha 1}$, $L_{\alpha 2}$, $L_{\beta 1}$, $L_{\beta 2}$, $L_{\gamma 1}$ and $M_{\alpha 1}$, and a total of 34 elements potentially present in spectra acquired from easel

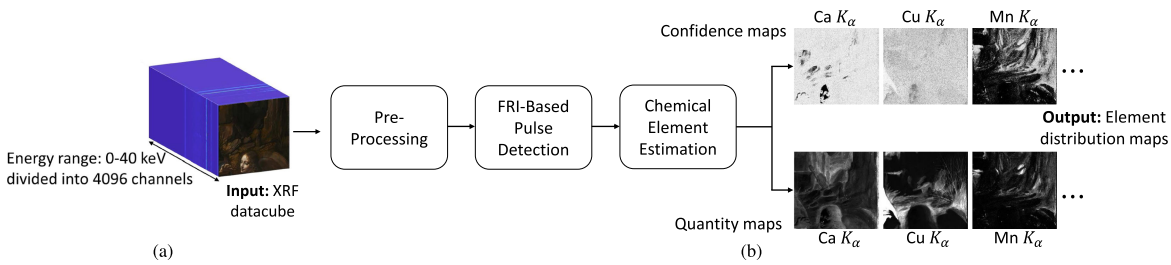

Fig. 3. (a) Representative MA-XRF datacube of an easel painting, with energy dimensions shown for a scan with a Bruker M6 JETSTREAM instrument. (b) The block diagram of our proposed approach for deconvolving the MA-XRF datacube of an easel painting.

paintings and detectable using the instrumentation described below [18]. Within the 11 characteristic X-rays, a number of the electronic transitions result in X-rays very close in energy and these are often considered as a single group when analysing the spectra. For example, $K_{\alpha 1}$ and $K_{\alpha 2}$ lines are often combined as K_α line group. Indeed for certain elements these X-rays are too close in energy to be separated using energy-dispersive XRF systems. Moreover, combining these X-rays can lead to a more insightful visualisation result when showing their distribution maps. This fusion results in 7 emission line groups, which are K_α, K_β, L_l, L_α, L_β, L_γ and M_α. Table I in Appendix C shows the details of the relevant characteristic X-rays of the 34 chemical elements considered.

B. MA-XRF Datasets

All the MA-XRF datasets included in this paper were acquired using the Bruker M6 JETSTREAM equipment at the National Gallery, London, with continuous scanning mode and the following settings: a 30 W rhodium (Rh) anode X-ray tube with polycapillary optics operated at 50 kV and 600 μA and a 60 mm^2 silicon (Si) drift detector with a threshold of 275 kcps. The resulting MA-XRF dataset from an easel painting is a three-dimensional datacube, with two spatial and one energy dimensions, as shown in Fig. 3(a). The range of the energy dimension is from 0 to 40 kilo-electron-volts (keV) and is divided into 4096 energy channels.

The radiation of each characteristic X-ray has a Lorentz distribution in the spectrum [9]. Moreover, due to the photon-to-charge conversion process in the MA-XRF detector, each characteristic X-ray will be convolved with a Gaussian-shaped response function [8]–[10]. Since the width of this response function is usually much larger than that of the Lorentz distribution, the shape of each characteristic X-ray in the spectrum can be modelled with a Gaussian function [9]. Therefore, the spectral response for each characteristic element X-ray takes the form of a Gaussian pulse covering a range of energies, as shown in Fig. 2(a), and the collected XRF spectrum of a pixel region can be modelled as a combination of several Gaussian pulses:

$$y[n] = \sum_{k=1}^{K} a_k \delta(n - t_k) \otimes \varphi(n; \sigma_k),\ n = 0, 1, ..., 4095, \quad (1)$$

where $\delta(.)$ represents the element lines, $\otimes$ is the convolution operator, n is the channel number, K is the total number of element lines in the spectrum, a_k and t_k are the amplitude and location of the k-th element line, $\varphi(n; \sigma_k)$ is the Gaussian pulse shape with variance of σ^2 given by:

$$\varphi(n; \sigma_k) = \exp\left(-\frac{n^2}{2\sigma_k^2}\right). \quad (2)$$

As the MA-XRF dataset is acquired pixel-wise, acquisition (or dwell) times per pixel tend to be short, often resulting in the XRF spectrum at each pixel having a poor signal-to-noise ratio, for example see Fig. 2(b). The amplitude noise in the XRF spectrum is due to the statistical nature of the counting process, in which random events (the arrival of X-ray photons at the detector) are observed during a finite time interval. For such a process, the probability of observing N counts when the 'true' number of counts is N_0 is given by the Poisson distribution: $P(N; N_0) = \frac{{N_0}^N}{N!} e^{-N_0}$. The number of counts in each channel of an X-ray spectrum as well as the sum over a number of channels obey this Poisson distribution. The statistical nature of the counting process (Poisson statistics or counting statistics) causes the typical channel to channel fluctuations observed in X-ray spectra [8].

C. MA-XRF Data Analysis

There are three major steps to a typical XRF analysis, after the system has been setup and the spectrum (or spectra) measured: (i) spectrum pre-processing to extract the characteristic X-rays from the detector response and spectral artefacts, as well as to relate channel index to X-ray energy level if this was not performed prior to acquisition; (ii) determination of the elements present and deconvolution of the characteristic X-rays to determine the analytically important net peak areas; and (iii) a quantification step in order to relate the net peak areas to the concentrations of the elements present, taking account of attenuation and matrix effects, normally involving some form of fundamental parameter calculations based on solving the Sherman equation [25]. With scanning MA-XRF systems creation of element distribution maps forms the final process. The algorithms used and the degree of operator intervention in these various steps depends on the software package used but in all standard approaches the user must specify the elements present.

For comparison with the results obtained using our proposed approach, each of the datasets acquired was also processed using the Bruker M6 software and using PyMca. In this study the method most commonly used in the heritage science field

was adopted using the Bruker M6 software [26]: (i) calibration using the zero strobe peak and a copper element standard; (ii) deconvolution of the 'sum' spectrum (the average spectrum of the entire datacube in the pixel domain) in order to determine which elements are believed to be present using an iterative quantification algorithm that forward calculates the resulting spectrum by repeatedly solving the Sherman equation; (iii) review of the 'maximum pixel spectrum' (an artificial spectrum that consists of the maximum content of every channel independent of the pixel) to try and identify any elements present in high abundance but in very localised areas that may be missed when fitting the sum spectrum and finally, (iv) based on the elements selected, distribution maps are created using the 'fast deconvolution' method which is based on a Bayesian fitting of the data in which every count in every channel is weighted by the probability that it belongs to one of the user-selected elements. While PyMca has the potential to give results that are believed to more accurately represent the various element distributions than it was possible to obtain directly from the Bruker M6 software using the method just described, its use requires a far greater degree of expert user intervention to produce these results. However, with the increasing adoption of MA-XRF scanning in the heritage science field, fewer and fewer of the users of this equipment within this field have the level of expertise required to use the PyMca software while the use of the Bruker M6 software is ubiquitous. It is for this reason that we chose, in the discussion that follows, to compare the results obtained using our algorithm with those obtained from the Bruker M6 software, despite this being a proprietary software.

D. Challenges in XRF Spectrum Deconvolution With MA-XRF Datasets Acquired From Easel Paintings

The Gaussian-shaped response of the XRF detector leads to the overlap of pulses associated with characteristic X-rays with similar energy levels. The fact that many pulses of different characteristic X-rays overlap makes it difficult to separate the response of different elements in the XRF spectrum and to map their independent distributions. Moreover:

1) The amplitudes (or intensities) of characteristic X-ray pulses vary greatly from a few photon counts up to hundreds due to the instrument settings and detector sensitivity. When a pulse with weak amplitude overlaps with a more intense pulse, it becomes difficult to detect the weak signal in the spectrum.
2) The width of the characteristic X-ray pulses increases with the photon energy [19], [27]. As the pulse shape changes across the spectrum, this imposes an extra difficulty in XRF deconvolution. The relationship between the full width at half maximum (FWHM) of a pulse and its characteristic energy E in electron-volts (eV) is given by [27]:

$$\text{FWHM} \propto \left(C^2 E + N^2\right)^{1/2}, \tag{3}$$

where C is the uncertainty in the formation of charge carriers and N is the electronic noise.

3) XRF spectra from individual pixels within an MA-XRF dataset having a poor signal-to-noise ratio, as shown in Fig. 2(b), making it challenging to detect pulses with small amplitudes. Moreover, the signals from elements associated with materials deep in the paint layer structure are partially attenuated by elements in the layers above and therefore a reduced number of photons produced by elements deep within the painting structure is detected.
4) The relative amplitudes of the set of characteristic X-rays for a given element may also change depending on where atoms of this element are within the layer structures of the scanned painting due to secondary effects [9]. For example, lower energy photons emitted by the atoms of a given element during ionisation are more likely than higher energy photons to be absorbed or scattered before reaching the detector. As a result, the relative amplitudes of sets of characteristic X-rays for an element in the observed spectrum may vary according to how deep the element is in the painting. This means that, unlike their energies (or pulse locations) which will not change, the relative amplitudes of the characteristic X-rays for a given element are variable and therefore the ratios of these amplitudes are not a reliable parameter for element identification.

III. Proposed Method

In Fig. 3 we show the block diagram of the proposed automatic approach for deconvolving the MA-XRF datacubes from easel paintings. The input is the MA-XRF datacube and the output is two sets of distribution maps (confidence maps and quantity maps) for all the chemical elements that are present in the painting. In what follows we first explain the pre-processing and calibration steps in Section III-A. Then in Section III-B, we explain our pulse detection algorithm which is able to retrieve the locations and amplitudes of the pulses from the XRF spectra using variations of FRI theory [20], [21] and Prony's method [22]. Finally in Section III-C, we show how we identify the chemical elements present in the painting and how we produce the corresponding distribution maps based on the retrieved pulses.

A. Pre-Processing and Calibration

The objective of the pre-processing step is to estimate the width of the characteristic X-ray pulses in the XRF spectra as well as relate the channel index of the detector with X-ray energy levels. To achieve this, the collected MA-XRF datacube is first averaged in the pixel domain to obtain the average spectrum of the entire datacube:

$$y_{\text{ave}}[n] = \frac{1}{I}\sum_{i=1}^{I} y_i[n],\ n = 0, 1, ..., 4095,$$

where y_i is the spectrum of pixel i and I is the number of pixels in the datacube. The following pre-processing steps operate on the average spectrum. Further, a 3-by-3-pixel moving average filter is applied on the MA-XRF datasets in this paper to help detect weak elements.

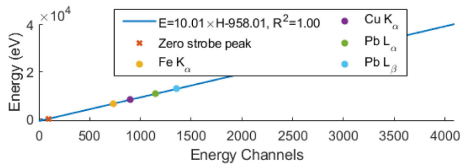

Fig. 4. Calibration of conversion between energy E and channel H.

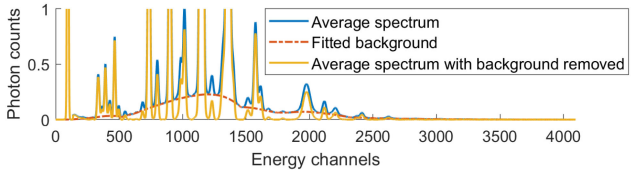

Fig. 5. Average spectrum with removal of background.

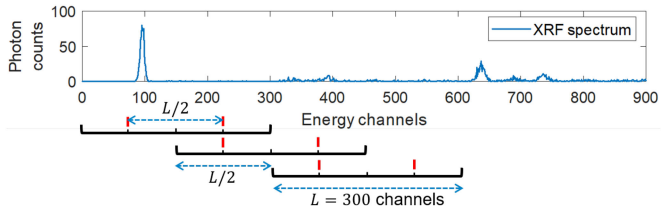

Fig. 6. The XRF spectrum is divided into overlapping windows with size $L = 300$ channels and the overlap between two consecutive windows is $L/2$. Red regions are confidence intervals with a size of $L/2$.

1) Reference Pulse Estimation: Firstly, a reference pulse is required. We normally pick the lowest channel pulse in the average spectrum to be the reference pulse because it always appears at the zero-energy level in the spectrum due to incomplete charge collection caused by detector imperfections [8], which is also known as the zero strobe peak. However, any pure pulse (a pulse having no overlap with others) in the average spectrum can be chosen as the reference pulse. We denote with $\{y_{\text{ref}}[n]\}$ the signal of this pulse. It has been discussed in Section II-B that the shape of the pulses in XRF spectra can be modelled with a Gaussian function. Therefore the reference pulse is fitted with a Gaussian using least-squares fitting to find its variance σ^2_{ref} and its location t_{ref}. Once σ_{ref} has been estimated, the full width at half maximum (FWHM) of the reference pulse is given by $\text{FWHM}_{\text{ref}} = 2\sqrt{2\ln 2}\sigma_{\text{ref}}$.

2) Energy-Channel Calibration: For each pixel of data, the multi-channel analyser of the MA-XRF device counts the number of received photons at different energy levels and indexes the energy levels using channel numbers. It is therefore necessary to match the channel numbers with the energy levels. This is achieved by exploiting the fact that the transformation that describes the mapping is normally linear so only two coefficients need to be estimated to describe it.

We achieve this by first using the fact that the reference pulse from the average spectrum is always at zero energy level. Then the characteristic X-rays of some elements that are often present with high intensities in easel paintings are identified manually from the average spectrum for calibration (for example, the X-ray emission lines of iron K_α, copper K_α, lead L_α and L_β as shown in Fig. 4). Linear least-squares regression is applied to fit the transformation between energy E and energy channels H. Note that this calibration is necessary regardless of the algorithm chosen (Bruker M6 software, PyMca, etc.) and is normally done once with a new device, as long as the scanning settings remain the same.

3) Background Removal: Because of scattering, photons are collected at all energy levels leading to a background signal which becomes significant when the XRF spectra are averaged. Since the sensitivity of the sensor in the detector varies with the energy level, the background noise is non-uniform across channels and has an effect on the shape of the pulses. Therefore a background removal method (SNIP) proposed in [28] is used here, which is to iteratively apply the following procedure on the average spectrum:

$$y^{(\varrho)}_{\text{back}}[n] = \min\left(\frac{y^{(\varrho-1)}_{\text{back}}[n-d] + y^{(\varrho-1)}_{\text{back}}[n+d]}{2}, y^{(\varrho-1)}_{\text{back}}[n]\right),$$

where $y^{(\varrho)}_{\text{back}}[n]$ represents the estimated background at the ϱ-th iteration and $y^{(0)}_{\text{back}}[n] = y_{\text{ave}}[n]$. 25 iterations and d as 10 times the FWHM of the reference pulse are good for the datasets collected with M6 instrument but might differ for other instruments. An example of an average spectrum with background removal is shown in Fig. 5. The average spectrum after background removal is given by $\hat{y}_{\text{ave}}[n] = y_{\text{ave}}[n] - y^{(25)}_{\text{back}}[n]$.

4) Pulse Width Estimation: As discussed in Section II-D, the FWHM of characteristic X-rays increases with energy following (3). The FWHM of a characteristic X-ray pulse at energy E can be calculated based on the given reference pulse in the average spectrum at energy $E_{\text{ref}} = 0$ with width FWHM_{ref} as [29]:

$$\text{FWHM} = \left(2.5\mu E + \text{FWHM}^2_{\text{ref}}\right)^{1/2}, \tag{4}$$

where μ is an added adjustment coefficient.

We estimate the adjustment coefficient μ using nonlinear least-square fitting. The estimation steps include first selecting a pure pulse (without any overlap with others) from the average spectrum after background removal, which is at energy channel H_{pure}, corresponding to energy level E_{pure}. The FWHM of the pure pulse ($\text{FWHM}_{\text{pure}}$) can be expressed using (4) and with $E = E_{\text{pure}}$. Then, since for a Gaussian function $\text{FWHM} = 2\sqrt{2\ln 2}\sigma$, μ can be retrieved by:

$$\hat{\mu} = \arg\min_{\mu,a} \sum_n \left\| a\exp\left(-\frac{(n-H_{\text{pure}})^2}{2\sigma^2_{\text{pure}(\mu)}}\right) - y_{\text{pure}}[n]\right\|^2_2,$$

where $\{y_{\text{pure}}[n]\}$ indicates the pure pulse signal. To reduce the estimation error, $\hat{\mu}$ can be picked by the average of fitting results based on multiple pure pulses.

B. FRI-Based Pulse Detection

Our proposed approach operates on the MA-XRF dataset pixel by pixel. We divide the XRF spectrum into overlapping windows of size $L = 300$ channels and the overlap between two consecutive windows is $L/2$, as shown in Fig. 6. We also have

a confidence interval (red regions in Fig. 6) with size $L/2$ and only keep the detected pulses inside it.

After removing the background for the XRF spectrum at each pixel with SNIP method, our pulse detection algorithm is then applied on the spectrum within each window. More importantly, by dividing the spectrum into windows with a relatively small size, we can assume that the pulse width remains the same within each window. Therefore, the spectrum can be modelled as a linear combination of several shifted Gaussian pulses with the same shape plus a noise term:

$$\hat{y}_j[n] = \sum_{k=1}^{K_j} a_{j,k}\varphi_j[n - t_{j,k}] + \epsilon_j[n], \tag{5}$$

where $n = jL, jL+1, ..., jL+L-1$, $\hat{y}_j[n]$ is the XRF spectrum in the j-th window of the pixel under consideration after the background removal, K_j is the number of pulses in the j-th window; $\{a_{j,k}\}_{k=1}^{K_j}$ and $\{t_{j,k}\}_{k=1}^{K_j}$ are the amplitudes and locations of the pulses; $\varphi_j[n]$ is the Gaussian pulse for the j-th window and $\epsilon_j[n]$ is the noise. The FWHM of the Gaussian pulse for the j-th window (FWHM$_j$) is calculated by (4) with energy level E_j converted from channel $H_j = jL + L/2$, the middle channel of the j-th window.

Given $\hat{y}_j[n]$, the XRF spectrum in (5) is completely specified by $\{t_{j,k}\}_{k=1}^{K_j}$ and $\{a_{j,k}\}_{k=1}^{K_j}$. For this reason the XRF spectrum in each window can be regarded as a signal with finite rate of innovation (FRI) [20] and the problem of estimating the $\{t_{j,k}\}$ and $\{a_{j,k}\}$ can be solved using FRI theory and a variant of Prony's method. We note that the accurate estimation of the locations $\{t_{j,k}\}$ is essential because they indicate the presence of a specific element line in the pixel. Likewise, the amplitudes $\{a_{j,k}\}$ are important as they are used for estimating the relative quantity of an element.

In order to estimate the free parameters in (5), we need to convert the sum of K_j Gaussian pulses into a sum of K_j exponentials so that Prony's method [22] or matrix pencil [30] can be applied. To this end, we leverage the "Approximate Strang-Fix" framework introduced in [21] and [31]. Specifically, we find coefficients $\{c_{j,m,n}\}$ such that linear combinations of uniformly shifted versions of the Gaussian pulse approximately reproduce complex exponentials. Given $\varphi_j(t) = \exp(-\frac{t^2}{2{\sigma_j}^2})$, we look for $\{c_{j,m,n}\}$ such that:

$$\sum_{n\in\mathbb{Z}} c_{j,m,n}\varphi_j(n-t) \approx e^{\mathrm{i}\omega_m t}, \tag{6}$$

for $\omega_m = \omega_0 + m\lambda$, $m = 0, 1, ..., M-1$, $\lambda = \frac{-2\omega_0}{M-1}$, where M is the highest order of exponentials that $\varphi_j(n)$ can reproduce and ω_0 is an arbitrary constant. We set $M = L$ and $\omega_0 = -0.35\pi$. Setting M equal to the number of samples is known to improve the performance of Prony's method, while ω_0 is chosen empirically. One way to estimate coefficients $\{c_{j,m,n}\}$ is fitting $\varphi_j(t)$ with an E-spline [32] and then computing

$$c_{j,m,n} = \frac{\hat{\phi}_j(\mathrm{i}\omega_m)e^{\mathrm{i}\omega_m n}}{\hat{a}_{\phi_j}(e^{-\mathrm{i}\omega_m})},$$

where $\phi_j(t)$ is the E-spline that best fits the Gaussian $\varphi_j(t)$, $\hat{\phi}_j(\mathrm{i}\omega_m)$ is the Fourier transform of $\phi_j(t)$ at $\mathrm{i}\omega_m$ and $\hat{a}_\phi(e^{\mathrm{i}\omega_m})$ is the z-transform of $a_{\phi_j}[l] = \langle\phi_j(t-l), \phi_j(t)\rangle$ evaluated at $z = e^{\mathrm{i}\omega_m}$ (see [21]) and is given by:

$$\hat{a}_{\phi_j}(e^{\mathrm{i}\omega_m}) = \sum_{l\in\mathbb{Z}} a_{\phi_j}[l]e^{-\mathrm{i}\omega_m l}.$$

Then we can multiply $\hat{y}_j[n]$ with $c_{j,m,n}$ to obtain:

$$\begin{aligned} s_j[m] &= \sum_n c_{j,m,n}\hat{y}_j[n] \\ &= \sum_{k=1}^{K_j} a_{j,k}\sum_n c_{j,m,n}\varphi_j[n - t_{j,k}]. \end{aligned} \tag{7}$$

Replacing (6) in (7) yields:

$$\begin{aligned} s_j[m] \approx \sum_{k=1}^{K_j} a_{j,k}e^{\mathrm{i}\omega_m t_{j,k}} &= \sum_{k=1}^{K_j} a_{j,k}e^{\mathrm{i}\omega_0 t_{j,k}}(e^{\mathrm{i}\lambda t_{j,k}})^m \\ &= \sum_{k=1}^{K_j} b_k {u_k}^m, \end{aligned} \tag{8}$$

where $b_k = a_{j,k}e^{\mathrm{i}\omega_0 t_{j,k}}$ and $u_k = e^{\mathrm{i}\lambda t_{j,k}}$. Therefore, the measurements $\hat{y}_j[n]$ are converted to a signal in the form of a sum of exponentials. The locations $\{t_{j,k}\}_{k=1}^{K_j}$ of the Gaussian pulses in the j-th window can be retrieved from the moments $s_j[m]$ with Prony's method [22] or matrix pencil [21], [30]. An overview of the basic Prony's method can be found in Appendix A. Given the retrieved $\{t_{j,k}\}_{k=1}^{K_j}$, we estimate the amplitude $\{a_{j,k}\}_{k=1}^{K_j}$ using least-squares fitting on (5).

Matrix pencil method requires the number of pulses K_j to be known, but our goal is to detect and localise an unknown number of potential pulses within each window. Leveraging the fact that matrix pencil is fast, we propose to solve this model selection problem by examining the number of pulses K_j from 1 to a maximum number $K_{\max}$. For any given K_j, the pulse locations $\{t_{j,k}\}_{k=1}^{K_j}$ and amplitudes $\{a_{j,k}\}_{k=1}^{K_j}$ are retrieved by matrix pencil and least-squares fitting. After that, the spectrum can be reconstructed and the mean absolute error MAE$_{j,K_j}$ between the reconstructed spectrum $\tilde{y}_{j,K_j}[n]$ and the original one $\hat{y}_j[n]$ is computed. The reason we use MAE here is to make the large pulses in the spectrum less dominant when computing reconstruction errors. With K_j increasing from 1 to $K_{\max}$, the MAE$_{j,K_j}$ gradually decreases because the spectrum can be better approximated. The reconstructed spectra with $K_j - 1$ and K_j pulses have the relationship:

$$\tilde{y}_{j,K_j}[n] \approx \tilde{y}_{j,K_j-1}[n] + a_{j,K_j}\varphi_j[n - t_{j,K_j}].$$

Thus, the MAE difference between $K_j - 1$ and K_j pulses is:

$$\begin{aligned} \Delta\mathrm{MAE}_{(K_j-1,K_j)} &= \mathrm{MAE}_{j,K_j-1} - \mathrm{MAE}_{j,K_j} \\ &\approx \frac{\sum_{n=jL}^{jL+L-1}|a_{j,K_j}\varphi_j[n - t_{j,K_j}]|}{L}. \end{aligned}$$

If we assume that K_j is the correct pulse number, then the $(\hat{K}_j + 1)$-th pulse starts fitting the background, that is $a_{j,K_j+1} < \varepsilon_j$,

Algorithm 1: FRI-Based Pulse Detection Algorithm.

Input: XRF spectrum of the i-th pixel, $y_i[n]$.
Output: The amplitudes and locations of the detected pulses for this pixel, $\{a_k\}_{k=1}^{K}$ and $\{t_k\}_{k=1}^{K}$.

for *window* $j \leftarrow 1$ **to** J **do**
  $\hat{y}_j[n] = y_i[n]$ after background noise removal, $n = jL, jL+1, ..., (j+1)L-1$.
  Compute the FWHM$_j$ and σ_j for the j-th window
  Calculate the coefficients $\{c_{j,m,n}\}$.
  Calculate the moments $\{s_j[m]\}$.
  for $K_j \leftarrow 1$ **to** $K_{\max}$ **do**
    Retrieve $\{t_{j,k}\}_{k=1}^{K_j}$ from $\{s_j[m]\}$.
    Retrieve $\{a_{j,k}\}_{k=1}^{K_j}$ with least-squares.
    Reconstruct the spectrum $\tilde{y}_{j,K_j}[n]$ and compute MAE$_{j,K_j}$.
    if $\Delta MAE_{(\hat{K}_j,\hat{K}_j+1)} < \xi_j$ **then**
      Keep the optimal detection results $\hat{K}_j$, $\{a_{j,k}\}_{k=1}^{\hat{K}_j}$ and $\{t_{j,k}\}_{k=1}^{\hat{K}_j}$.
      Break the **for loop** 6.
  Apply confidence interval and obtain $\{\check{a}_{j,k}\}_{k=1}^{\check{K}_j}$, $\{\check{t}_{j,k}\}_{k=1}^{\check{K}_j}$ and $\check{K}_j$.
$\{a_k\}_{k=1}^{K} = \left\{\{\check{a}_{j,k_j}\}_{k_j=1}^{\check{K}_j}\right\}_{j=1}^{J}$,
$\{t_k\}_{k=1}^{K} = \left\{\{\check{t}_{j,k_j}\}_{k_j=1}^{\check{K}_j}\right\}_{j=1}^{J}$ and $K = \sum_{j=1}^{J}\check{K}_j$.

where ε_j is the background level for the j-th window and is given by:

$$\varepsilon_j = \frac{\sum_{n=jL}^{jL+L-1} y_{\text{back}}^{(25)}[n]}{L}.$$

Therefore, we decide that $\hat{K}_j$ is the correct number when $\Delta\text{MAE}_{(\hat{K}_j,\hat{K}_j+1)}$ is smaller than the threshold

$$\xi_j = \frac{\sum_{n=jL}^{jL+L-1} |\varepsilon_j \varphi_j[n - t_\varepsilon]|}{L}$$

with $t_\varepsilon = jL + L/2$. Then a confidence interval with $L/2$ length located in the middle of the window is applied and we denote with $\{\check{a}_{j,k}\}_{k=1}^{\check{K}_j}$, $\{\check{t}_{j,k}\}_{k=1}^{\check{K}_j}$ and $\check{K}_j$ the amplitudes, locations and number of detected pulses inside the confidence interval of the j-th window. After the detection algorithm has been applied on all windows of a pixel, the detected pulses for the entire spectrum are given by the set of all amplitudes and locations detected in each window and are denoted with $\{a_k\}_{k=1}^{K}$ and $\{t_k\}_{k=1}^{K}$ respectively, where $K = \sum_{j=1}^{J}\check{K}_j$ is the number of detected pulses for the spectrum at this pixel. Finally, the algorithm is performed on all pixels of the dataset. Our pulse detection algorithm is summarised in Algorithm 1.

C. Chemical Element Estimation

Given the locations $\{t_k\}$ and the amplitudes $\{a_k\}$ of the pulses, we now need to assign the detected pulses to the correct characteristic X-ray emission lines in order to determine which chemical elements are present at a certain pixel and their intensities. Let us introduce two parameters to quantify the presence of a chemical element, which are confidence score and quantity score. The confidence score represents the confidence that we have correctly allocated a pulse to a certain chemical element at a specific pixel and is a value that ranges from zero to one. The quantity score represents the measured intensity of that element at that pixel location.

As previously noted in Section II-A, the characteristic X-rays emitted by a chemical element are often combined into emission line groups for better visualisation results. On this basis, we first compute the confidence and quantity scores for the 11 dominant characteristic X-ray lines of a chemical element to yield line confidence scores (LCS) and line quantity scores (LQS). These are then combined to compute the confidence and quantity scores for the 7 emission line groups of that element to yield group confidence scores (GCS) and group quantity scores (GQS). Finally, the confidence and quantity distribution maps for a line group of an element are produced by showing its GCS and GQS values for all the pixels.

1) Line Confidence Score and Line Quantity Score: We construct a look up matrix with the corresponding energy channels of the characteristic X-rays for the 34 chemical elements considered (see Appendix C), represented by $\boldsymbol{H} \in \mathbb{R}^{P\times Q}$. Here, $P = 34$ denotes the number of elements and $Q = 11$ denotes the maximum number of characteristic X-rays considered for each element. With the proposed FRI-based pulse detection algorithm, K pulses $\{(t_k, a_k)\}_{k=1}^{K}$ have been detected from the XRF spectrum of a certain pixel. Therefore, we use $\boldsymbol{V} \in \mathbb{R}^{K\times P\times Q}$ to represent all the LCS.

We define the LCS for a single characteristic X-ray of an element as the difference in energy level (measured in channels) between the detected pulse and the characteristic X-ray and is given by:

$$v_{k,p,q} = \max\left(1 - \frac{|t_k - H_{p,q}|}{\tau_k}, 0\right), \tag{9}$$

where $v_{k,p,q}$ represents the LCS computed for the k-th detected pulse and the q-th characteristic X-ray of the p-th element, τ_k is an uncertainty factor that depends on the amplitude a_k of the detected pulse. As the photon counting process in the XRF device follows a Poisson distribution, a pulse with large amplitude has a high signal-to-noise ratio. Therefore, its detection result is expected to be more accurate and is associated with a smaller uncertainty factor τ_k. The way in which we derive the dependency of τ_k on a_k is explained in Appendix B and is based on Cramér-Rao bounding techniques [23]. Fig. 7(a) illustrates how the LCS is computed. Moreover, two constraints are imposed when assigning detected pulses to chemical elements: a) When a characteristic X-ray of an element has non-zero LCS with more than one detected pulse, the highest LCS is kept and the others are set to zero. This is to ensure that only the closest detected pulse is assigned to each characteristic X-ray. b) When a detected pulse has non-zero LCS with respect to more than one characteristic X-ray of the same element, the highest LCS is kept and the others are set to zero. This is to ensure that one

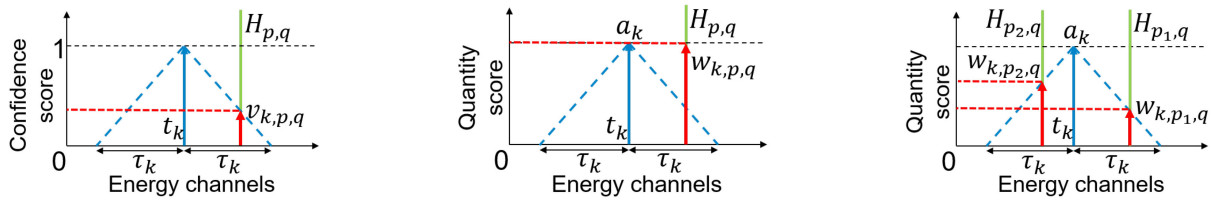

(a) LCS (b) LQS without overlap (c) LQS in case of overlap

Fig. 7. Computation of LCS and LQS. The green lines represent the locations (energy channels) of the characteristic X-ray $H_{p,q}$. The blue arrow represents the location of the detected pulse t_k. The blue dashed lines represent the confidence score function defined in (9). The red arrow in (a) denotes the computed LCS $v_{k,p,q}$ and the red arrows in (b) and (c) are LQS $w_{k,p,q}$. The value of τ_k depends on the estimated amplitude a_k of the pulse and τ_k is smaller when a_k is larger (details of how τ_k is computed are provided in Appendix B).

detected pulse can only be assigned to one characteristic X-ray of a certain element.

Similarly, we use $\boldsymbol{W} \in \mathbb{R}^{K\times P\times Q}$ to represent all the possible LQS. The LQS of a single characteristic X-ray of an element depends on the amplitudes of the detected pulses that have been allocated to that element. Two cases are considered: a) when a detected pulse has been allocated to only one characteristic X-ray, then the LQS equals to the amplitude of the allocated pulse, as shown in Fig. 7(b); b) when a detected pulse has been allocated to multiple elements, the LQS between the detected pulse and those characteristic X-rays is defined as the pulse amplitude multiplied by the corresponding LCS, as shown in Fig. 7(c). Therefore, the LQS for the q-th characteristic X-ray of the p-th element computed with the k-th detected pulse is:

$$w_{k,p,q} = \begin{cases} a_k, \text{ if } \forall(\bar{p}\neq p,\bar{q}) : v_{k,\bar{p},\bar{q}} = 0, \\ a_k v_{k,p,q}, \text{ if } \exists(\bar{p}\neq p,\bar{q}) : v_{k,\bar{p},\bar{q}} > 0. \end{cases} \tag{10}$$

We also note that with the two constraints applied to the LCS, only one pulse can be allocated to a characteristic X-ray of an element, which means that there is only one non-zero value in both $\boldsymbol{V}_{:,p,q}$ and $\boldsymbol{W}_{:,p,q}$. As a consequence, $\boldsymbol{V}$ and $\boldsymbol{W}$ can be compressed into two two-dimensional matrices, $\tilde{\boldsymbol{V}} \in \mathbb{R}^{P\times Q}$ and $\tilde{\boldsymbol{W}} \in \mathbb{R}^{P\times Q}$, as follows:

$$\tilde{v}_{p,q} = \sum_k v_{k,p,q} \text{ and } \tilde{w}_{p,q} = \sum_k w_{k,p,q}, \tag{11}$$

where $\tilde{v}_{p,q}$ and $\tilde{w}_{p,q}$ represent the LCS and LQS for the q-th characteristic X-ray of the p-th element, respectively.

2) Group Confidence Score and Group Quantity Score: Given the LCS and LQS in (11), we then combine them to compute the GCS and GQS of the 7 emission line groups (K_α, K_β, L_l, L_α, L_β, L_γ, M_α) for the 34 elements described previously. We use $\hat{\boldsymbol{V}} \in \mathbb{R}^{P\times R}$ and $\hat{\boldsymbol{W}} \in \mathbb{R}^{P\times R}$ to represent all the GCS and GQS respectively, where $R = 7$ is the number of emission line groups considered for each element.

Since, within each line group, the first characteristic X-ray (e.g. $K_{\alpha 1}$ within the K_α line group) is more likely to be emitted than the others, its pulse in the XRF spectrum is normally more intense and more likely to be detected. Therefore, we define the GCS of a group as the maximum between the LCS of this dominant characteristic X-ray and the averaged LCS of all the characteristic X-rays in that group:

$$\hat{v}_{p,r} = \max\left(\tilde{v}_{p,q_{r1}}, \frac{1}{|Q_r|}\sum_{q\in Q_r}\tilde{v}_{p,q}\right), \tag{12}$$

where $\hat{v}_{p,r}$ represents the GCS for the r-group of the p-th element, Q_r is the set of characteristic X-rays in the r-group and q_{r1} represents the first characteristic X-ray in the r-group. The GQS of a group is defined as the sum of the LQS of all the characteristic X-rays in that group:

$$\hat{w}_{p,r} = \sum_{q\in Q_r}\tilde{w}_{p,q}, \tag{13}$$

where $\hat{w}_{p,r}$ is the GQS for the r-group of the p-th element.

The characteristic X-rays of an element are generated in series (e.g. K-series, L-series, M-series, etc.) and the combined emission of the characteristic X-rays in the α-group is the most prevalent in each line series, generally resulting in higher intensity in the XRF spectrum. As such the GCS and GQS in a series of an element are adjusted according to the GCS and GQS of the α-group. Since the combined intensity of the α-group is normally at least twice that of any other group in the series, the GQS of any other groups larger than the α-group is adjusted to half of the GQS of the α-group. Furthermore, if no detected pulse has been allocated to the X-ray lines in the α-group, resulting in a zero GCS and a zero GQS, it can be almost certain that the X-ray lines of other groups in that series will not be present in the spectrum. In this case, the GCS of all other groups in that series are set to zero. These adjustments can be summarised as:

$$\begin{cases} \hat{w}_{p,r} = \frac{\hat{w}_{p,r_{G\alpha}}}{2}, \text{ if } r\in R_G \text{ and } \hat{w}_{p,r} > \hat{w}_{p,r_{G\alpha}} \\ \{\hat{v}_{p,r}\}_{r\in R_G} = 0, \text{ if } \hat{v}_{p,r_{G\alpha}} = 0 \text{ and } \hat{w}_{p,r_{G\alpha}} = 0 \end{cases} \tag{14}$$

where R_G is the set of line groups in the G-series and $r_{G\alpha}$ is the α-group in the G-series. We also note that the arsenic (As) K_α and lead (Pb) L_α lines are very difficult to separate. The detection of As is therefore treated in a different way from all other elements and is the only case where the K_β lines are considered when determining if As is present. Only when As K_β lines are detected in the spectra do we consider As K_α lines to be present in the spectrum. Moreover, the ratio between the summed intensities of As K_β lines and K_α lines is set as 1:6.

3) GQS Refinement: The method in Sections III-C1 and III-C2 gives us, through the GCS, reliable information about

Algorithm 2: Chemical Element Estimation Algorithm.

Input: The detected pulses from the XRF spectra, with amplitudes and locations $\{a_k, t_k\}_{k=1}^{K}$.
Output: Elemental distribution maps (the GCS maps and GQS maps) for all elements present.
Compute $\boldsymbol{V}$ (LCS) and $\boldsymbol{W}$ (LQS) for each detected pulse using (9) and (10).
Convert $\boldsymbol{V}$ and $\boldsymbol{W}$ into two-dimensional matrices with (11) to obtain $\tilde{\boldsymbol{V}}$ and $\tilde{\boldsymbol{W}}$.
Compute $\hat{\boldsymbol{V}}$ (GCS) and $\hat{\boldsymbol{W}}$ (GQS) with (12) and (13).
Adjust $\hat{\boldsymbol{V}}$ and $\hat{\boldsymbol{W}}$ with (14).
Obtain all the characteristic lines of the elements that have at least one non-zero GCS, represented with the locations $\{\tilde{t}_k\}_{k=1}^{\tilde{K}}$.
Re-apply the least-squares fitting on the XRF spectrum to obtain the corresponding amplitudes $\{\tilde{a}_k\}_{k=1}^{\tilde{K}}$.
Follow Steps 1-4 to obtain the refined GQS ($\bar{\boldsymbol{W}}$).
Generate two sets of elemental distribution maps by showing $\hat{\boldsymbol{V}}$ (GCS) and $\bar{\boldsymbol{W}}$ (GQS) for all pixels.

which chemical elements are present in the XRF spectrum at a certain pixel in the dataset. However, the pulses detected from the spectrum may have errors in amplitude and location and this can cause errors when calculating the GQS. To reduce this problem, we refine the GQS of the potential elements leveraging the exact locations of their characteristic lines. At this refinement stage, if any of the characteristic X-rays in an element series are detected, it is assumed that all of the characteristic X-rays of that element contribute to the spectrum and the locations of all of these lines are included in the fitting.

As in Section III-B, each spectrum is divided into L-length overlapping windows and an $L/2$-length confidence interval is applied to each window. We denote the number of characteristic lines in the j-th window as $K_{\psi,j}$ and the locations of these lines as $\{\hat{t}_{j,k}\}_{k=1}^{K_{\psi,j}}$. By replacing the pulse locations $\{t_{j,k}\}_{k=1}^{K_j}$ in (5) with $\{\hat{t}_{j,k}\}_{k=1}^{K_{\psi,j}}$, the corresponding amplitudes of these characteristic lines can be re-estimated from the spectrum with least-squares fitting. As some of the characteristic lines are close to others, their estimated amplitudes may be negative and they can be regarded as redundant lines. We therefore remove those lines and repeat the fitting until all the remaining lines have positive amplitudes. Then, we only keep those characteristic lines inside the confidence interval. Combining the re-estimation results for all windows gives the locations ($\{\tilde{t}_k\}_{k=1}^{\tilde{K}}$) and amplitudes ($\{\tilde{a}_k\}_{k=1}^{\tilde{K}}$) of the remaining characteristic lines for the whole spectrum. With $\{\tilde{t}_k\}_{k=1}^{\tilde{K}}$ and $\{\tilde{a}_k\}_{k=1}^{\tilde{K}}$, the GQS of potential elements, represented by $\bar{\boldsymbol{W}} \in \mathbb{R}^{P\times R}$, can be re-computed following the steps in Sections III-C1 and III-C2.

4) Element Distribution Map: Finally, the distribution maps are generated for each chemical element present in the dataset by showing the GCS ($\hat{\boldsymbol{V}}$) and GQS ($\bar{\boldsymbol{W}}$) for all the pixels in the datacube. The procedure for generating the element distribution maps is summarised in Algorithm 2.

Fig. 8. Vincent van Gogh, *Sunflowers* (NG3863), 1888. Oil on canvas [33], [34]. ©The National Gallery, London. Highlighted is the region scanned with a Bruker M6 JETSTREAM instrument (580 μm spot size, 580 μm step size, 10 ms dwell time).

IV. Numerical Results

In this section, the performance of our proposed algorithm is assessed with MA-XRF datacubes acquired from three easel paintings in the National Gallery collection.[1] The element distribution maps produced by our algorithm are compared with those produced using the Bruker M6 software. This software, as is typical of other methods mentioned in Section I, requires user input to determine which elements are present before distribution maps are created. Further, with these methods, the appearance of individual element maps produced from a given dataset can vary depending on the precise elements chosen to include. By contrast, our method generates the distribution maps automatically (after some essential pre-processing and calibration steps) and, as shown in this section, is able to find weak element signals within a dataset and separate (or deconvolute) characteristic X-rays with similar energies but related to different elements.

A. Automatic Element Distribution Map Generation

We first verify the ability of our algorithm to automatically detect the chemical elements present in the painting and the additional benefits of producing a confidence map.

A region of the painting *Sunflowers* painted by Vincent van Gogh, highlighted in Fig. 8 [33], [34], was scanned and the resulting MA-XRF dataset was processed with our proposed algorithm to generate the distribution maps of the chemical elements that are present in the painting. Fig. 9 illustrates the confidence maps and quantity maps of the major emission line groups of a representative selection of elements extracted by our algorithm. Compared with the quantity maps produced using the Bruker M6 software shown in Fig. 10, our quantity maps show similar distributions. However, due to the large dynamic range of measured intensities, it is not always easy to confirm the presence of a certain element by just inspecting the quantity

[1]The results obtained from Titian's *Diana and Callisto* (NG6616) are presented in the supplementary material.

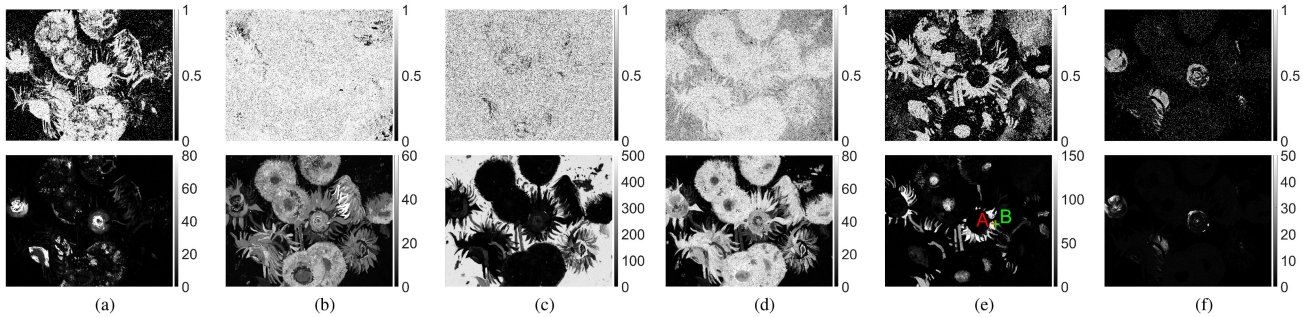

Fig. 9. Confidence maps (in the first row) and quantity maps (in the second row) of the major emission line groups of example chemical element produced by our algorithm for the scanned region of *Sunflowers*. (a) Iron (Fe) K_α, (b) Chromium (Cr) K_α, (c) Zinc (Zn) K_α, (d) Lead (Pb) L_β, (e) Copper (Cu) K_α, and (f) Bromine (Br) K_α. Highlighted in the Cu K_α quantity map are two sample pixels *A* and *B*.

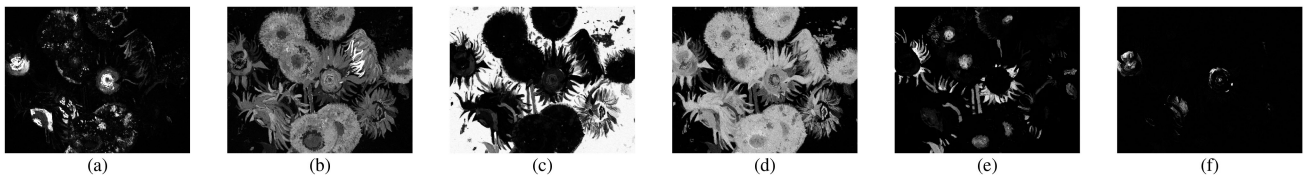

Fig. 10. Quantity maps of the major emission line groups of example chemical element produced using Bruker M6 software (after deconvolution) for the scanned region of *Sunflowers*. (a) Iron (Fe) K_α, (b) Chromium (Cr) K_α, (c) Zinc (Zn) K_α, (d) Lead (Pb) L_β, (e) Copper (Cu) K_α, and (f) Bromine (Br) K_α.

maps. For instance, it is not clear whether iron (Fe) exists in some areas of the flower petals (rather than just in the centres of the flowers) when only looking at the quantity maps of Fe K_α (Fig. 9(a) second row and 10(a)). In this case, our confidence map (Fig. 9(a) first row) indicates that most of the petals have confidence values approaching 1, suggesting that Fe does exist in those areas with high probability but the quantity could be very low. We would like to highlight that the confidence maps that are produced automatically by our algorithm could alert users to the presence of low intensity signal, which they could then further interrogate with image manipulation such as log scaling or, indeed, evaluation of individual spectra.

The presence of some Fe in the petals, sepals and foliage has been confirmed by detailed examination of the painted surface or analysis of cross-section samples, showing that the additional information provided by the confidence maps can help heritage scientists to confirm whether particular elements, and hence materials, are present at particular locations in easel paintings. The situation is similar with the low proportion of bromine (Br) detected in the centres of the flowers and linked to the use of a type of pigment known as geranium lake (a red pigment based on the organic red colorant eosin, a bromine derivative of fluorescein) [34].

Then to demonstrate the ability of our algorithm to automatically detect the chemical elements present in the painting, we focus on two sample pixels (*A* and *B*) on the yellow-green sepal on the right of central sunflower, highlighted in Fig. 9(e), which are close to where a micro-sample was taken from the painting. This sample was prepared as a cross-section and analysed using scanning electron microscopy with energy-dispersive X-ray analysis (SEM-EDX) [33], [34]. This analysis revealed that in the area of the yellow-green sepal there is a ground layer containing lead white ($2PbCO_3 \cdot Pb(OH)_2$), then a layer that may be underdrawing executed with a material that is mainly carbon-based and not

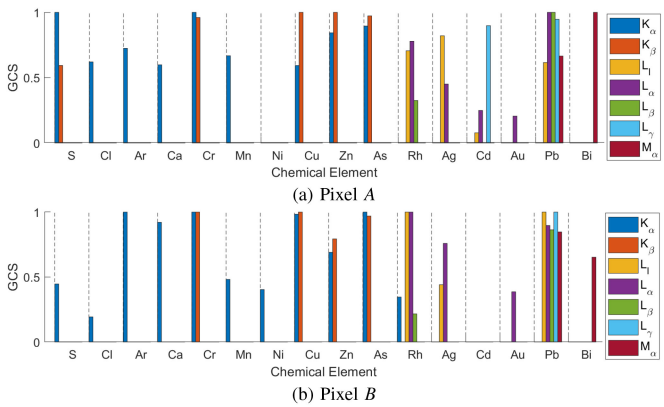

Fig. 11. GCS of the chemical elements detected by our algorithm at (a) pixel *A* and (b) pixel *B*, where Pb, Cu, As, Cr, Ca, Zn and S are expected to be present. Ar and Rh appear systematically in all spectra acquired with this device.

detected by MA-XRF scanning and finally a layer containing a mixture of emerald green ($3Cu(AsO_2)_2 \cdot Cu(CH_3COO)_2$), chrome yellow ($PbCrO_4 \cdot PbCr_{1-x}S_xO_4$, where $0 < x < 1$), calcium sulphate ($CaSO_4 \cdot 2H_2O$) and some zinc white (ZnO). Therefore, the chemical elements present in this area are expected to be lead (Pb), copper (Cu), arsenic (As), chromium (Cr), calcium (Ca), zinc (Zn) and sulphur (S). Fig. 11 shows the GCS of all the chemical elements that are detected by our algorithm at the sample pixels *A* and *B*. It can be seen that all of the expected elements are detected with high GCS, especially for their major emission line groups.

As already noted and discussed, the algorithm is deliberately designed to detect elements present in low quantity and in Fig. 11 a number of other elements are reported as having generally low but non-zero GCS values. While this has the potential to result in 'false positive' element identifications, this does not negatively affect the distribution maps of the other elements that

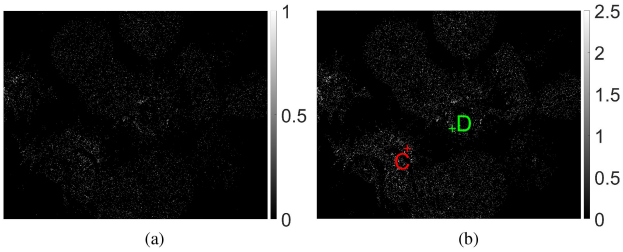

Fig. 12. Distribution maps of mercury (Hg) L_α emission line group produced by our algorithm for the scanned region of *Sunflowers*; (a) Confidence map, (b) Quantity map. Highlighted are two sample pixels *C* and *D*.

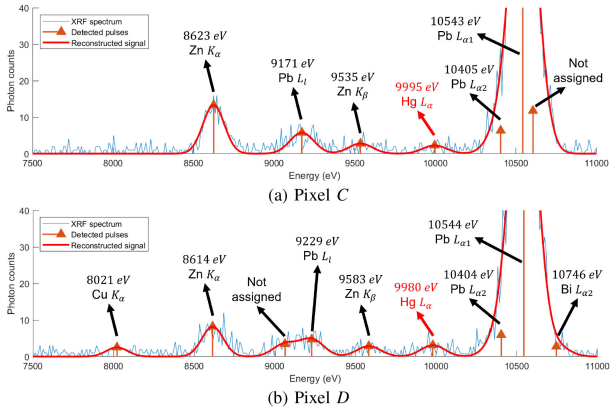

Fig. 13. Pulse detection results produced by our algorithm at (a) pixel *C* and (b) pixel *D* in the scanned region of *Sunflowers*.

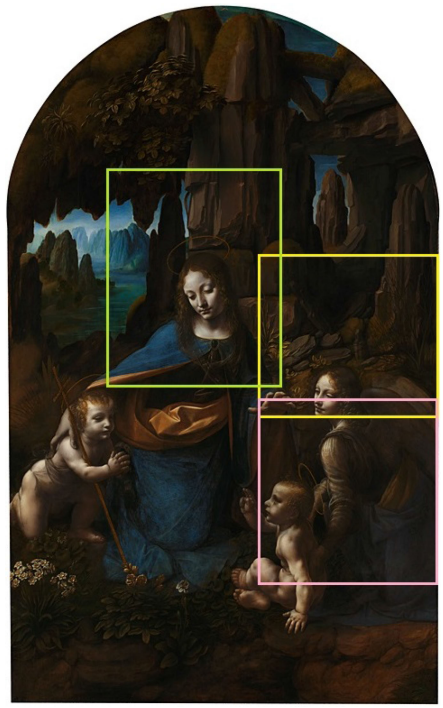

Fig. 14. Leonardo da Vinci, *The Virgin with the Infant Saint John the Baptist adoring the Christ Child accompanied by an Angel ('The Virgin of the Rocks')* (NG1093), about 1491/2-9 and 1506-8. Oil on poplar, thinned and cradled [35]. ©The National Gallery, London. Highlighted are three regions scanned with a Bruker M6 JETSTREAM instrument (350 μm spot size, 350 μm step size and 10 ms dwell time).

are confirmed to be present and by examining which emission lines have been detected, generally spectroscopists can quite easily identify such cases. Further, the quantity maps associated with the unexpected elements at sample pixels *A* and *B* (Ag, Cd, Au and Bi) are generally very low. More importantly, unlike other existing methods, our algorithm does not require users to input which elements are expected but provides the estimation automatically with high accuracy. This is also highlighted in Fig. 13(a) where a Bi $L_{\alpha2}$ false positive is avoided. This happens because the pulse detected is relative large and the corresponding uncertainty bound stops us from assigning it to a not too close element line.

B. Weak Signal Detection

As has been discussed earlier, the XRF spectra collected from paintings using an MA-XRF scanning device can be very noisy, leading to a challenge of detecting characteristic X-rays of chemical elements of low intensities from the noisy spectra. We demonstrate that our proposed algorithm is able to detect weak signals from the noisy XRF spectra.

For example, our algorithm manages to detect the element mercury (Hg), whose presence in the painting could not be confirmed when analysing the dataset with the Bruker M6 software, but now has been validated [33], [34]. Using optical microscopy and Raman spectroscopy, the presence of the mercury-containing pigment vermilion, or mercury sulphide (HgS), has been confirmed in paint cross-sections. The distribution maps of the Hg L_α line group produced by our algorithm are shown in Fig. 12. In the confidence map (Fig. 12(a)), some pixels with confidence values around 0.4 can be seen roughly coinciding with the centres of some of the sunflowers. The quantity map (Fig. 12(b)) indicates similar regions with quantity values of about 2 photon counts. These same areas can also be seen in the confidence and quantity maps for the Hg L_β line group. To further validate the accuracy of these findings, we now focus on two sample pixels *C* and *D*, highlighted in Fig. 12(b). The $L_{\alpha1}$ and $L_{\alpha2}$ emission lines of Hg are expected at energies about 9989 eV and 9898 eV. When the intensity of Hg is weak as in the pulses selected, only the dominant $L_{\alpha1}$ line is detectable in the spectrum. The pulse detection results in Fig. 13 indicate that one pulse at 9995 eV with amplitude 2.27 and one at 9980 eV with amplitude 3.11 are detected at pixels *C* and *D*, respectively, corresponding to the Hg $L_{\alpha1}$ line.

There are three reasons why the detection of Hg is particularly challenging in this MA-XRF dataset: (i) Hg is present in small amounts; (ii) the L-series lines of Hg overlap with many lines of other elements (e.g. As, Br); (iii) the L-series lines of Hg are located in the parts of XRF spectra where great background noise exists. Despite these challenges, our algorithm is still able to detect Hg correctly.

C. Revealing Hidden Drawings in Leonardo's Masterpiece

Several pairs of chemical elements, such as zinc (Zn) and copper (Cu), have characteristic X-rays with similar energies such that their signals in the XRF spectrum partially overlap in energy, making them difficult to separate. Cu has K_α and K_β lines expected at energies of about 8041 eV and 8905 eV and Zn

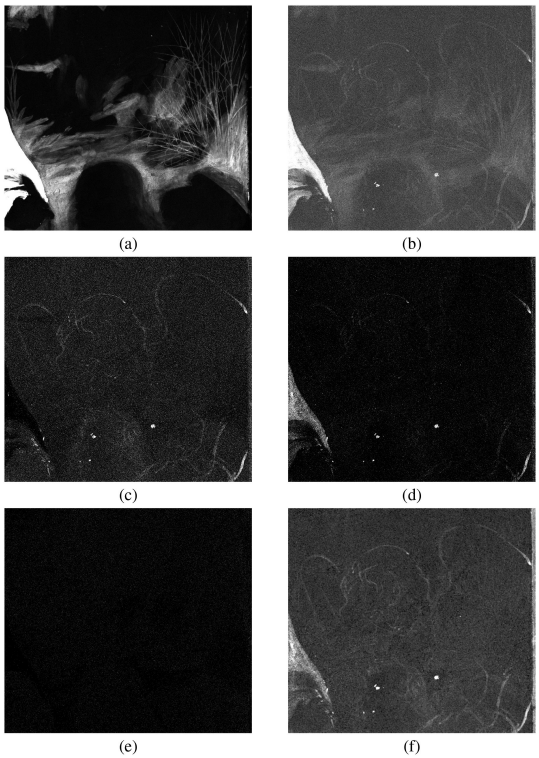

Fig. 15. Quantity maps produced by Bruker M6 software for the scanned region (yellow outline) of *'The Virgin of the Rocks'*. (a) Cu K_α after deconvolution, (b) Zn K_α region of interest, (c) Zn K_α after deconvolution without Ni added in the element list, (d) Zn K_α after deconvolution with Ni added in the element list, (e) Ni K_α after deconvolution with Ni added in the element list, and (f) Zn K_α with Cu K_α manually subtracted and 3-by-3 binning.

has K_α and K_β lines expected at energies of about 8631 eV and 9572 eV, respectively. Because the Cu K_β line is close in energy to the Zn K_α line, it is difficult to separate the signal from these two elements in XRF spectra, especially when one is much stronger than the other. The datasets collected on the painting *'The Virgin of the Rocks'* by Leonardo da Vinci present this separation challenge. The highlighted areas in Fig. 14 represent three MA-XRF datasets collected with a Bruker M6 JETSTREAM MA-XRF instrument. These datasets were analysed using the Bruker M6 software to produce the quantity maps of Cu K_α (Fig. 15(a)) and Zn K_α (Fig. 15(b)). It can be seen that there is significant interference due to Cu in the Zn map if regions of interest are used without further deconvolution. Fig. 16 illustrates the distribution maps of Cu K_α and Zn K_α extracted by our algorithm. Our Cu K_α confidence map (Fig. 16(a)) has values close to 1 at most of the pixels, suggesting that copper is present throughout this particular region of the painting. Our Cu K_α map (Fig. 16(b)) is similar to the one produced using the Bruker M6 software, showing clear bright regions that correspond to the Virgin's drapery and the foliage in the painting. This indicates that the intensities of Cu at the pixels of the areas of foliage and especially for the pixels of the drapery on the left side of the dataset are much higher than in the other areas. Previous examination found that the Virgin's drapery was underpainted with the copper-containing pigment azurite, whilst the foliage includes another copper-based pigments, verdigris [35].

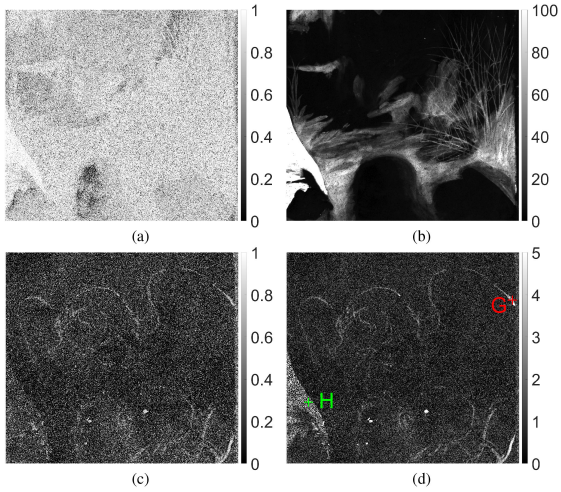

Fig. 16. Distribution maps of copper (Cu) K_α and zinc (Zn) K_α emission line groups produced by our algorithm for the scanned region (yellow outline) of *'The Virgin of the Rocks'*. (a) Cu K_α confidence map, (b) Cu K_α quantity map, (c) Zn K_α confidence map, and (d) Zn K_α quantity map. Highlighted are two sample pixels *G* and *H*.

The distribution maps of Zn K_α produced by our algorithm show unexpected results and the quantity map is quite different to that produced using the Bruker M6 software. Some pixels with GCS about 0.8 in our Zn K_α confidence map (Fig. 16(c)) create what appear to be lines, which are even more clear in our Zn K_α quantity map (Fig. 16(d)). These Zn-containing features do not correspond to any visible composition in the painting. Instead, they are related to underdrawing of planned figures (the wings and the head of an angel are clearly visible) that was then painted over. Although previous technical examination of the painting had revealed the existence of underdrawing for an unrealised figure of the Virgin, the planned figures of the angel and Christ child were unknown prior to undertaking the MA-XRF scanning [35], [36].

It is also of interest to note that photon counts for the lines of the underdrawing are very low and yet our method has been able to find the signal related to Zn, the presence of which was confirmed using SEM-EDX in a micro-sample of paint mounted in cross-section. Our Zn K_α quantity map also indicates that the azurite pigment used in the underlayer for the Virgin's drapery contains a little Zn which has also been confirmed in another cross-section using SEM-EDX.

Using the inbuilt deconvolution algorithm in the Bruker M6 software, a Zn K_α quantity map (Fig. 15(c)) is produced that allows this underdrawing to be seen more easily without the overlap from Cu-containing regions. Significantly, however, the Zn K_α signal in the Virgin's drapery is entirely removed during this deconvolution and the residual Zn signal is very weak. In an attempt to avoid this issue, an expert user must manually scale and subtract the Cu map (Fig. 15(a)) from the Zn map (Fig. 15(b)) to obtain a result believed to accurately reflect the distribution of Zn (Fig. 15(f)). Furthermore, adding the element nickel (Ni), which is not likely to be present in the painting, to the list of the selected chemical elements leads to a deconvoluted map (Fig. 15(d)) that inverts the signal of Zn in the robes of the Virgin, even though Zn and Ni have no overlapping peaks. This demonstrates that the selection of elements for the M6 software

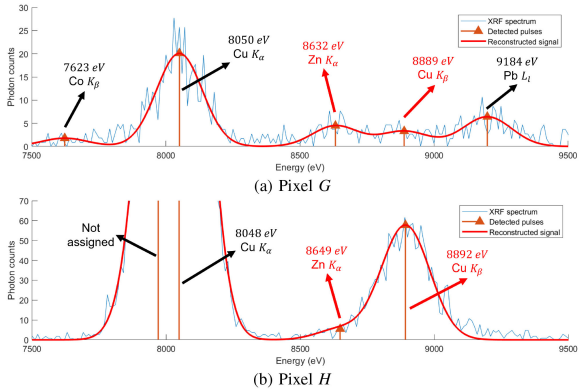

Fig. 17. Pulse detection results produced by our algorithm at (a) Pixel G and (b) Pixel H in the scanned region (yellow outline) of *'The Virgin of the Rocks'*.

Fig. 18. Combined Zn K_α quantity map produced by our algorithm for the three scanned regions of *'The Virgin of the Rocks'*, revealing underdrawing related to an abandoned earlier composition.

by the user does have a strong effect on the accuracy of the XRF deconvolution results. In contrast, our algorithm is able to reveal the underdrawing and an accurate Zn quantity map in an automated manner.

To verify the accuracy of our algorithm, we focus on pixels G on the angel wing and H on the drapery highlighted in Fig. 16(d). The pulse detection results of these two sample pixels are shown in Fig. 17. For pixel G, two pulses detected at 8050 eV and 8889 eV relate to Cu and one pulse detected at 8632 eV to Zn. For pixel H, two detected pulses at 8048 eV and 8892 eV correspond to Cu and one pulse at 8649 eV relates to Zn. These results reveal the excellent ability of our algorithm to detect nearby pulses from noisy spectra, even when the weak pulse is partially covered by a much stronger one.

Finally, a combined Zn K_α quantity map produced by our algorithm for the three scanned regions of *'The Virgin of the Rocks'* is shown in Fig. 18 and reveals the complexity of the abandoned composition with sketches of the Virgin and Christ Child also appearing. More importantly, when used on these three different datasets, our algorithm gives consistent results so that they can be combined easily, showing no obvious borders or discontinuities, which is further evidence of the stability and accuracy of the proposed method.

V. Conclusion

In this paper, we have proposed an automatic approach for extracting elemental maps from MA-XRF datasets acquired from easel paintings, with some essential pre-processing steps. Two distribution maps, a confidence and a quantity map, are produced to detect and quantify the presence of chemical elements in the paintings. To demonstrate the performance of the proposed approach, we tested it on MA-XRF datasets from three easel paintings at the National Gallery in London and the resulting distribution maps are compared with those produced using the Bruker M6 software. The results confirm the ability of our method to automatically generate element distribution maps, even when detecting very weak element signals within noisy datasets and when separating overlapping element pulses, and the value of having both the confidence and quantity maps to review. Furthermore, the zinc-containing underdrawing hidden in *'The Virgin of the Rocks'* by Leonardo da Vinci is successfully revealed by our approach with great clarity and without any additional user intervention.

Appendix A
Prony's Method

Prony's method was developed in 1795 by Baron de Prony for the original purpose of estimating the frequency, phase and amplitude parameters of a finite sum of sinusoids [22]. In the last several decades, Prony's method has been rediscovered and extended many times in different fields. For example, it can be used in parametric sampling theory [20], [37] and also to solve some inverse problems [38]–[40]. In what follows, we present a simple derivation of the basic Prony's method.

To start, we have obtained from (8) that $s[m]$ is the sum of K exponentials:

$$s_m = \sum_{k=1}^{K} a_k e^{\mathrm{i}\omega_0 t_k} (e^{\mathrm{i}\lambda t_k})^m = \sum_{k=1}^{K} b_k u_k^m, \tag{15}$$

where $b_k = a_k e^{\mathrm{i}\omega_0 t_k}$ and $u_k = e^{\mathrm{i}\lambda t_k}$. Assuming that the sparsity level K is known, we aim to retrieve the coefficients $\{b_k\}$ and the exponentials $\{u_k\}$ from $2K$ consecutive elements $\{s_m : \ell \leq$

$m < \ell + 2K\}$. The locations $\{t_k\}_{k=1}^K$ and amplitudes $\{a_k\}_{k=1}^K$ of the Gaussian pulses can then be reconstructed from $\{b_k\}$ and $\{u_k\}$.

The key to Prony's method is a clever use of the algebraic structure of the expression in (15). Let

$$P(x) = \prod_{k=1}^{K}(x - u_k) = x^K + h_1 x^{K-1} + ... + h_{K-1}x + h_K$$

be a Kth order polynomial whose roots are $\{u_k\}$. Then, it is easy to verify that

$$s_{m+K} + h_1 s_{m+K-1} + ... + h_K s_m = \sum_{1 \le k \le K} b_k u_k^m P(u_k) = 0.$$

Writing this identity in matrix-vector form for all indices m such that $\ell \le m < \ell + K$, we get

$$0 = \begin{pmatrix} s_{\ell+K} & s_{\ell+K-1} & \cdots & s_\ell \\ s_{\ell+K+1} & s_{\ell+K} & \cdots & s_{\ell+1} \\ \vdots & \vdots & \ddots & \vdots \\ s_{\ell+2K-1} & s_{\ell+2K-2} & \cdots & s_{\ell+K-1} \end{pmatrix} \begin{pmatrix} 1 \\ h_1 \\ \vdots \\ h_K \end{pmatrix} \stackrel{\text{def}}{=} \boldsymbol{T}_{K,\ell}\boldsymbol{h}, \tag{16}$$

where, by construction, $\boldsymbol{T}_{K,\ell}$ is a Toeplitz matrix of size $K \times (K+1)$.

The above equation reveals that the vector of polynomial coefficients $\boldsymbol{h} = (1, h_1, ..., h_K)^T$ is in the null space of $\boldsymbol{T}_{K,\ell}$. Next, we show that this condition is sufficient to uniquely identify $\boldsymbol{h}$.

Proposition 1: Suppose that $b_k \neq 0$ for all k and that the K parameters $\{u_k\}$ are distinct. Then

$$\text{rank}(\boldsymbol{T}_{K,\ell}) = K.$$

Proof: We can decompose the Toeplitz matrix $\boldsymbol{T}_{K,\ell}$ as:

$$\boldsymbol{T}_{K,\ell} = \boldsymbol{B}\boldsymbol{A}\boldsymbol{C},$$

where $\boldsymbol{A} \stackrel{\text{def}}{=} \text{diag}(b_0 u_0^\ell, b_1 u_1^\ell, ..., b_{K-1} u_{K-1}^\ell)$, $\boldsymbol{B}$ is the Vandermonde matrix of size $K \times K$ given by

$$\boldsymbol{B} \stackrel{\text{def}}{=} \begin{pmatrix} 1 & 1 & \cdots & 1 \\ u_0^1 & u_1^1 & \cdots & u_{K-1}^1 \\ \vdots & \vdots & \ddots & \vdots \\ u_0^{K-1} & u_1^{K-1} & \cdots & u_{K-1}^{K-1} \end{pmatrix},$$

and $\boldsymbol{C}$ is a second Vandermonde matrix of size $K \times (K+1)$ and of the form

$$\boldsymbol{C} \stackrel{\text{def}}{=} \begin{pmatrix} u_0^K & u_0^{K-1} & \cdots & 1 \\ u_1^K & u_1^{K-1} & \cdots & 1 \\ \vdots & \vdots & \ddots & \vdots \\ u_{K-1}^K & u_{K-1}^{K-1} & \cdots & 1 \end{pmatrix}.$$

Since the coefficients $\{b_k\}_{k=0}^{K-1}$ are nonzero, the diagonal matrix $\boldsymbol{A}$ is invertible. Furthermore, since the parameters $\{u_k\}_{k=0}^{K-1}$ are distinct, both Vandermonde matrices $\boldsymbol{B}$ and $\boldsymbol{C}$ have rank K. It follows that $\boldsymbol{T}_{K,\ell}$ has also rank K, and thus its null space is of dimension one. We can therefore conclude that vector $\boldsymbol{h}$ is the unique vector satisfying the identity (16).

In light of the above derivations, we summarise Prony's method as follows:

1) Given the input s_m, build the Toeplitz matrix $\boldsymbol{T}_{K,\ell}$ as in (16) and solve for $\boldsymbol{h}$. This can be achieved by taking the SVD of $\boldsymbol{T}_{K,\ell}$ and choosing as $\boldsymbol{h}$ the (scaled) right-singular vector associated with the zero singular value. The scaling is done so that the first element of $\boldsymbol{h}$ is equal to 1.
2) Find the roots of $P(x) = 1 + \sum_{k=1}^K h_k x^{K-k}$, which are exactly the exponentials $\{u_k\}_{k=0}^{K-1}$.
3) Given the parameters $\{u_k\}_{k=0}^{K-1}$, find the corresponding weights $\{b_k\}_{k=0}^{K-1}$ by solving K linear equations as given in (15). This is a Vandermonde system of equations which yields a unique solution for the weights $\{b_k\}_{k=0}^{K-1}$ since $\{u_k\}_{k=0}^{K-1}$ are distinct.

Described above is the basic Prony's method. There are variations of this method that lead to better detection results, for instance, the matrix pencil method [21], [30]. These methods are normally based on constructing matrices larger than the one in (16).

APPENDIX B
CRAMÉR-RAO LOWER BOUND FOR GAUSSIAN PULSE ESTIMATION WITH POISSON NOISE

We leverage Cramér-Rao lower bounding techniques [23] to determine the uncertainty factor τ_k in (9). The amplitudes $\{a_k\}$ and locations $\{t_k\}$ of the element pulses are the parameters to be estimated and the Cramér-Rao lower bound (CRLB) provides the best achievable estimation performance.

Let $\boldsymbol{Y} = \{Y_n\}_{n=0}^{L-1}$ and $\boldsymbol{y} = \{y[n]\}_{n=0}^{L-1}$ denote the random XRF spectrum and the observation in one window with size L respectively. According to Section III-B, the observed spectrum in each window can be modelled as the combination of several Gaussian pulses with same shape plus random noise:

$$y[n] = x[n, \boldsymbol{\theta}] + \epsilon[n] = \sum_{k=1}^{K} a_k \varphi_j[n - t_k] + \epsilon[n], \tag{17}$$

where $x[n, \boldsymbol{\theta}]$ represents the theoretical noiseless spectrum, $\boldsymbol{\theta}$ represents the set of parameters to be estimated given by:

$$\boldsymbol{\theta} = \{\theta_i\}_{i=1}^{2K} = (a_1, a_2, ..., a_K, t_1, t_2, ..., t_K)^T, \tag{18}$$

K is the pulse number, $\epsilon[n]$ is the random noise and $\varphi[n]$ is the Gaussian pulse given by $\varphi[n] = \exp\left(-\frac{n^2}{2\sigma^2}\right)$. The noise is due to the statistical nature of the counting process, in which random events (the arrival of X-ray photons at the detector) are observed during a finite time interval [8]. Therefore, the spectrum sample Y_n at each energy channel follows the Poisson distribution [41], that is, $Y_n \sim \text{Pois}(x[n, \boldsymbol{\theta}])$ and the probability density function (pdf) of Y_n is thus given by

$$p_{Y_n}(y[n]; \boldsymbol{\theta}) = p_{Y_n}(y[n]; x[n, \boldsymbol{\theta}]) = \frac{x[n, \boldsymbol{\theta}]^{y[n]} e^{-x[n, \boldsymbol{\theta}]}}{y[n]!}.$$

If the XRF spectrum samples are independent, the pdf of $\boldsymbol{Y} = \{Y_n\}_{n=0}^{L-1}$ is given by the product of the pdf of each Y_n:

$$p_{\boldsymbol{Y}}(\boldsymbol{y};\boldsymbol{\theta}) = \prod_{n=0}^{L-1} p_{Y_n}(y[n];\boldsymbol{\theta}) = \prod_{n=0}^{L-1} \frac{x[n,\boldsymbol{\theta}]^{y[n]} e^{-x[n,\boldsymbol{\theta}]}}{y[n]!}.$$

The log-likelihood function depending on $\boldsymbol{\theta}$, given $\boldsymbol{Y} = \boldsymbol{y}$ and $Y_n = y[n]$, is expressed as:

$$\ell(\boldsymbol{\theta};\boldsymbol{y}) = \sum_{n=0}^{L-1} y[n] \ln\left(x[n,\boldsymbol{\theta}]\right) - x[n,\boldsymbol{\theta}] - \ln\left(y[n]!\right).$$

The derivative of $\ell(\boldsymbol{\theta};\boldsymbol{y})$ with respect to each θ_i is

$$\frac{\partial \ell(\boldsymbol{\theta};\boldsymbol{y})}{\partial \theta_i} = \sum_{n=0}^{L-1} \left(\frac{y[n]}{x[n,\boldsymbol{\theta}]} - 1\right) \frac{\partial x[n,\boldsymbol{\theta}]}{\partial \theta_i}.$$

So the gradient of $\ell(\boldsymbol{\theta};\boldsymbol{y})$ with respect to $\boldsymbol{\theta}$ is

$$\nabla \ell(\boldsymbol{\theta};\boldsymbol{y}) = \sum_{n=0}^{L-1} \left(\frac{y[n]}{x[n,\boldsymbol{\theta}]} - 1\right) \nabla x[n,\boldsymbol{\theta}].$$

The Fisher information matrix is then given by:

$$\begin{aligned}\boldsymbol{I}(\boldsymbol{\theta}) &= \mathbb{E}\{\nabla \ell(\boldsymbol{\theta};\boldsymbol{Y})(\nabla \ell(\boldsymbol{\theta};\boldsymbol{Y}))^T\} \\ &= \sum_{n=0}^{L-1}\sum_{m=0}^{L-1} \left(\frac{\mathbb{E}\{Y_n Y_m\}}{x[n,\boldsymbol{\theta}]x[m,\boldsymbol{\theta}]} - \frac{\mathbb{E}\{Y_n\}}{x[n,\boldsymbol{\theta}]} - \frac{\mathbb{E}\{Y_m\}}{x[m,\boldsymbol{\theta}]} + 1\right) \\ &\qquad \times \nabla x[n,\boldsymbol{\theta}](\nabla x[m,\boldsymbol{\theta}])^T. \quad (19)\end{aligned}$$

Since $Y_n \sim \text{Pois}(x[n,\boldsymbol{\theta}])$, $Y_m \sim \text{Pois}(x[m,\boldsymbol{\theta}])$, $\mathbb{E}\{Y_n\} = x[n,\boldsymbol{\theta}]$, and $\mathbb{E}\{Y_m\} = x[m,\boldsymbol{\theta}]$, (19) becomes:

$$\boldsymbol{I}(\boldsymbol{\theta}) = \sum_{n=0}^{L-1}\sum_{m=0}^{L-1} s_{n,m}(\boldsymbol{\theta}) \nabla x[n,\boldsymbol{\theta}](\nabla x[m,\boldsymbol{\theta}])^T,$$

$$\text{where } s_{n,m}(\boldsymbol{\theta}) = \frac{\mathbb{E}\{Y_n Y_m\}}{x[n,\boldsymbol{\theta}]x[m,\boldsymbol{\theta}]} - 1.$$

$\mathbb{E}\{Y_n Y_m\}$ can be expressed as:

$$\mathbb{E}\{Y_n Y_m\} = \begin{cases} \text{cov}(Y_n, Y_m) + \mathbb{E}\{Y_n\}\mathbb{E}\{Y_m\}, & n \neq m, \\ \text{var}(Y_n) + \mathbb{E}\{Y_n\}^2, & n = m. \end{cases}$$

Since $Y_n \sim \text{Pois}(x[n,\boldsymbol{\theta}])$ and samples $(Y_n)_{n=0}^{L-1}$ are assumed to be independent, we have that $\text{cov}(Y_n, Y_m) = 0$ when $n \neq m$ and $\text{var}(Y_n) = x[n,\boldsymbol{\theta}]$. So $\mathbb{E}\{Y_n Y_m\}$ can be written as:

$$\mathbb{E}\{Y_n Y_m\} = \begin{cases} x[n,\boldsymbol{\theta}]x[m,\boldsymbol{\theta}], & n \neq m, \\ x[n,\boldsymbol{\theta}] + x[n,\boldsymbol{\theta}]^2, & n = m. \end{cases}$$

Then we obtain:

$$s_{n,m}(\boldsymbol{\theta}) = \begin{cases} 0, & n \neq m, \\ \frac{1}{x[n,\boldsymbol{\theta}]}, & n = m. \end{cases}$$

Therefore, the Fisher information matrix $\boldsymbol{I}(\boldsymbol{\theta})$ becomes:

$$\boldsymbol{I}(\boldsymbol{\theta}) = \sum_{n=0}^{L-1} \frac{1}{x[n,\boldsymbol{\theta}]} \nabla x[n,\boldsymbol{\theta}](\nabla x[n,\boldsymbol{\theta}])^T.$$

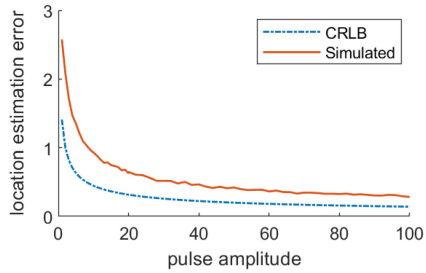

Fig. 19. Performance of our FRI-based pulse detection algorithm to estimate 1 pulse from a $L = 300$ length signal in the presence of Poisson noise. The pulse shape is a Gaussian function with standard deviation $\sigma = 5$. The location of the pulse is fixed at the centre of the window.

From (18) and (17), $\nabla x[n,\boldsymbol{\theta}]$ can be derived as:

$$\nabla x[n,\boldsymbol{\theta}] = \begin{pmatrix} \varphi[n-t_1] \\ \vdots \\ \varphi[n-t_K] \\ -a_1 \frac{\partial \varphi[n-t_1]}{\partial t_1} \\ \vdots \\ -a_K \frac{\partial \varphi[n-t_K]}{\partial t_K} \end{pmatrix} = \begin{pmatrix} \nu_1[n] \\ \vdots \\ \nu_K[n] \\ \gamma_1[n] \\ \vdots \\ \gamma_K[n] \end{pmatrix},$$

where $\nu_j[n] = \varphi[n-t_j]$, $\gamma_j[n] = -a_j \frac{\partial \varphi[n-t_j]}{\partial t_j}$ and $j = 1, 2, ..., K$. Thus the Fisher information matrix $\boldsymbol{I}(\boldsymbol{\theta})$ is a $2K \times 2K$ matrix:

$$\boldsymbol{I}(\boldsymbol{\theta}) = \sum_{n=0}^{L-1} \frac{1}{x[n,\boldsymbol{\theta}]} \begin{pmatrix} \boldsymbol{R}(\boldsymbol{\nu},\boldsymbol{\nu}) & \boldsymbol{R}(\boldsymbol{\nu},\boldsymbol{\gamma}) \\ \boldsymbol{R}(\boldsymbol{\gamma},\boldsymbol{\nu}) & \boldsymbol{R}(\boldsymbol{\gamma},\boldsymbol{\gamma}) \end{pmatrix}$$

with

$$\boldsymbol{R}(\boldsymbol{\nu},\boldsymbol{\gamma}) = \begin{pmatrix} \nu_1[n]\gamma_1[n] & \cdots & \nu_1[n]\gamma_K[n] \\ \vdots & \ddots & \vdots \\ \nu_K[n]\gamma_1[n] & \cdots & \nu_K[n]\gamma_K[n] \end{pmatrix}.$$

Then the CRLB is given by the inverse of the Fisher information matrix: $\boldsymbol{P} = [\boldsymbol{I}(\boldsymbol{\theta})]^{-1}$.

We then implement the experiment of detecting 1 pulse fixed at the centre of the window with size $L = 300$. Fig. 19 compares the estimation performance of our algorithm with the CRLB for the pulse amplitude increasing from 1 to 100. The CRLB and the numerical results suggest that detecting a weaker pulse has a larger average estimation error. Although the performance of our method on the real XRF spectrum is worse than CRLB, its behaviour is still in line with the CRLB. Therefore, CRLB provides a good guideline on how estimation errors change with the pulse amplitudes. We thus define the uncertainty factor τ_k based on the calculated CRLB:

$$\tau_k = \max(\min(\eta P_{t_k}(\sigma_{\text{ref}}, a_k), \tau_{\max}), \tau_{\min}),$$

where σ_{ref} is the standard deviation of the reference pulse (the first pulse in the average spectrum), P_{t_k} is the CRLB calculated for the location of the k-th detected pulse given the amplitude a_k, η is a scale factor, $\tau_{\max}$ and $\tau_{\min}$ are the maximum and minimum values that τ_k can reach. We determine that good values are $\eta =$

13, $\tau_{\max} = 3.5$ and $\tau_{\min} = 10.5$ through experiments on three MA-XRF datasets.

APPENDIX C

TABLE I
ENERGIES OF THE CHARACTERISTIC X-RAYS OF 34 CHEMICAL ELEMENTS COMMONLY PRESENT IN SPECTRA ACQUIRED FROM EASEL PAINTINGS SUCH AS THOSE CONSIDERED IN THIS STUDY (IN EV). ITALICISED AR, ZR AND RH APPEAR SYSTEMATICALLY IN ALL SPECTRA ACQUIRED WITH THE BRUKER M6 JETSTREAM EQUIPMENT. THOSE LINES OUTSIDE THE DETECTION RANGE OF THE MA-XRF DEVICE HAVE BEEN REMOVED. TABLE TAKEN AND MODIFIED FROM [42]

		K series				*L* series						*M* series
		K_α group		K_β group		L_l group	L_α group		L_β group		L_γ group	M_α group
Element	Atomic No.	$K_{\alpha 1}$	$K_{\alpha 2}$	$K_{\beta 1}$	$K_{\beta 2}$	L_l	$L_{\alpha 1}$	$L_{\alpha 2}$	$L_{\beta 1}$	$L_{\beta 2}$	$L_{\gamma 1}$	$M_{\alpha 1}$
Al	13	1487		1557		/	/	/	/	/	/	/
Si	14	1740		1836		/	/	/	/	/	/	/
P	15	2014		2139		/	/	/	/	/	/	/
S	16	2307		2464		/	/	/	/	/	/	/
Cl	17	2622		2816		/	/	/	/	/	/	/
Ar	*18*	*2957*		*3191*		/	/	/	/	/	/	/
K	19	3313		3590		/	/	/	/	/	/	/
Ca	20	3690		4013		/	/	/	/	/	/	/
Ti	22	4509		4932		/	/	/	/	/	/	/
V	23	4950		5427		/	/	/	/	/	/	/
Cr	24	5412		5947		/	/	/	/	/	/	/
Mn	25	5895		6490		/	/	/	/	/	/	/
Fe	26	6400		7058		/	/	/	/	/	/	/
Co	27	6925		7649		/	/	/	/	/	/	/
Ni	28	7472		8265		/	/	/	/	/	/	/
Cu	29	8041		8905		/	/	/	/	/	/	/
Zn	30	8631		9572		/	/	/	/	/	/	/
As	33	10544	10508	11726	11864	/	/	/	/	/	/	/
Se	34	11222	11181	12496	12652	/	/	/	/	/	/	/
Br	35	11924	11878	13291	13470	/	/	/	/	/	/	/
Sr	38	14165	14098	15836	16085	1582	1806		1872		/	/
Zr	*40*	*15775*	*15691*	*17668*	*17970*	*1792*	*2042*		*2124*	*2219*	*2303*	/
Rh	*45*	*20216*	*20074*	*22724*	*23173*	*2377*	*2695*		*2834*	*3001*	*3144*	/
Ag	47	22163	21990	24942	25456	2634	2982		3151	3348	3520	/
Cd	48	23174	22984	26096	26644	2767	3131		3317	3528	3717	/
Sn	50	25271	25044	28486	29109	3045	3441		3663	3905	4131	/
Sb	51	26359	26111	29726	30390	3189	3602		3844	4101	4348	/
I	53	28612	28317	32295	33042	3485	3934		4221	4508	4801	/
Ba	56	32194	31817	36378	37257	3954	4466	4451	4828	5157	5531	/
Au	79	/	/	/	/	8494	9713	9628	11442	11585	13382	2123
Hg	80	/	/	/	/	8721	9989	9898	11823	11924	13830	2195
Pb	82	/	/	/	/	9185	10552	10450	12614	12623	14764	2346
Bi	83	/	/	/	/	9420	10839	10731	13024	12980	15248	2423
U	92	/	/	/	/	11618	13615	13439	17220	16428	20167	3171

REFERENCES

[1] S. Yan, J. Huang, N. Daly, C. Higgitt, and P. L. Dragotti, "Revealing hidden drawings in Leonardo's 'the virgin of the Rocks' from macro X-Ray fluorescence scanning data through element line localisation," in *Proc. IEEE Int. Conf. Acoust., Speech Signal Process.*, 2020, pp. 1444–1448.

[2] X. Huang, E. Uffelman, O. Cossairt, M. Walton, and A. K. Katsaggelos, "Computational imaging for cultural heritage: Recent developments in spectral imaging, 3-D surface measurement, image relighting, and X-Ray mapping," *IEEE Signal Process. Mag.*, vol. 33, no. 5, pp. 130–138, Sep. 2016.

[3] A. Pizurica *et al.*, "Digital image processing of the Ghent Altarpiece: Supporting the painting's study and conservation treatment," *IEEE Signal Process. Mag.*, vol. 32, no. 4, pp. 112–122, Jul. 2015.

[4] S. Huang, B. Cornelis, B. Devolder, M. Martens, and A. Pizurica, "Multimodal target detection by sparse coding: Application to paint loss detection in paintings," *IEEE Trans. Image Process.*, vol. 29, pp. 7681–7696, Jul. 2020.

[5] Q. Dai, E. Pouyet, O. Cossairt, M. Walton, F. Casadio, and A. Katsaggelos, "X-Ray fluorescence image super-resolution using dictionary learning," in *Proc. IEEE 12th Image, Video, Multidimensional Signal Process. Workshop*, 2016, pp. 1–5.

[6] Q. Dai, E. Pouyet, O. Cossairt, M. Walton, and A. K. Katsaggelos, "Spatial-Spectral representation for X-Ray fluorescence image super-resolution," *IEEE Trans. Comput. Imag.*, vol. 3, no. 3, pp. 432–444, Sep. 2017.

[7] Q. Dai, H. Chopp, E. Pouyet, O. Cossairt, M. Walton, and A. K. Katsaggelos, "Adaptive image sampling using deep learning and its application on X-Ray fluorescence image reconstruction," *IEEE Trans. Multimedia*, vol. 22, no. 10, pp. 2564–2578, Oct. 2020.

[8] R. Van Grieken and A. Markowicz, *Handbook of X-Ray Spectrometry*. New York, NY, USA: Marcal Dekker, 2001.

[9] B. Beckhoff *et al.*, *Handbook of Practical X-Ray Fluorescence Analysis*. Berlin, Germany: Springer, 2007.

[10] D. H. Wilkinson, "Breit-Wigners viewed through Gaussians," *Nuclear Instrum. Methods*, vol. 95, no. 2, pp. 259–264, 1971.

[11] P. Van Espen *et al.*, "A computer analysis of X-Ray fluorescence spectra," *Nucl. Instrum. Methods*, vol. 142, no. 1/2, pp. 243–250, 1977.

[12] B. Vekemans *et al.*, "Comparison of several background compensation methods useful for evaluation of energy-dispersive X-Ray fluorescence spectra," *Spectrochimica Acta Part B: At. Spectrosc.*, vol. 50, no. 2, pp. 149–169, 1995.

[13] B. Vekemans *et al.*, "Analysis of X-Ray spectra by iterative least squares (AXIL): New developments," *X-Ray Spectrometry*, vol. 23, no. 6, pp. 278–285, 1994.

[14] V. A. Solé *et al.*, "A multiplatform code for the analysis of energy-dispersive X-Ray fluorescence spectra," *Spectrochimica Acta Part B: At. Spectrosc.*, vol. 62, no. 1, pp. 63–68, 2007.

[15] M. Alfeld and K. Janssens, "Strategies for processing mega-pixel X-Ray fluorescence hyperspectral data: A case study on a version of Caravaggio's painting Supper at Emmaus," *J. Anal. At. Spectrometry*, vol. 30, no. 3, pp. 777–789, 2015.

[16] C. Ryan and D. Jamieson, "Dynamic analysis: on-line quantitative PIXE microanalysis and its use in overlap-resolved elemental mapping," *Nuclear Instrum. Methods Phys. Res. Sect. B: Beam Interact. Mater. At.*, vol. 77, no. 1/4, pp. 203–214, 1993.

[17] C. Ryan *et al.*, "A new method for on-line true-elemental imaging using PIXE and the proton microprobe," *Nuclear Instruments Methods Phys. Res. Sect. B: Beam Interact. Mater. At.*, vol. 104, no. 1–4, pp. 157–165, 1995.

[18] M. Alfeld *et al.*, "A mobile instrument for in situ scanning macro-XRF investigation of historical paintings," *J. Anal. At. Spectrometry*, vol. 28, no. 5, pp. 760–767, 2013.

[19] D. M. Conover, "Fusion of reflectance and X-Ray fluorescence imaging spectroscopy data for the improved identification of artists' materials," Ph.D. dissertation, The George Washington University, Washington, D.C., USA, 2015.

[20] M. Vetterli, P. Marziliano, and T. Blu, "Sampling signals with finite rate of innovation," *IEEE Trans. Signal Process.*, vol. 50, no. 6, pp. 1417–1428, Jun. 2002.

[21] J. A. Urigüen, T. Blu, and P. L. Dragotti, "FRI sampling with arbitrary Kernels," *IEEE Trans. Signal Process.*, vol. 61, no. 21, pp. 5310–5323, Nov. 2013.

[22] G. R. de Prony, "Essai éxperimental et analytique: Sur les lois de la dilatabilité de fluides élastique et sur celles de la force expansive de la vapeur de l'alkool,a différentes températures," *J. de l'École Polytechnique*, vol. 1, no. 22, pp. 24–76, 1795.

[23] P. Stoica *et al.*, *Spectral Analysis of Signals*. Upper Saddle River, NJ, USA: Pearson Prentice Hall, 2005.

[24] A. C. Thompson *et al.*, *X-Ray Data Booklet*. Lawrence Berkeley National Laboratory, University of California Berkeley, CA, USA, 2001, vol. 8, no. 4.

[25] R. M. Rousseau and J. A. Boivin, "The fundamental algorithm: A natural extension of the Sherman equation, Part I: theory," *Rigaku J.*, vol. 15, no. 1, pp. 13–135, 1998.

[26] R. Tagle *et al.*, "Processing of MA(or μ)-XRF data with the M6 software," in *Proc. 24th Int. Congr. X-Ray Opt. Microanal. (ICXOM24)*, 2017.

[27] J. I. Goldstein *et al.*, *Scanning Electron Microscopy and X-Ray Microanalysis*. Berlin, Germany: Springer, 2017.

[28] C. Ryan *et al.*, "SNIP, a statistics-sensitive background treatment for the quantitative analysis of PIXE spectra in geoscience applications," *Nuclear Instrum. Methods Phys. Res. Sect. B: Beam Interact. Mater. At.*, vol. 34, no. 3, pp. 396–402, 1988.

[29] C. E. Fiori and D. E. Newbury, "Artifacts observed in energy dispersive X-Ray spectrometry in the scanning electron microscope," *Scanning Electron Microsc.*, vol. 1, no. 1978, pp. 401–422, 1978.

[30] Y. Hua and T. K. Sarkar, "Matrix pencil method for estimating parameters of exponentially damped/undamped sinusoids in noise," *IEEE Trans. Acoust., Speech, Signal Process.*, vol. 38, no. 5, pp. 814–824, May 1990.

[31] X. Wei and P. L. Dragotti, "Universal sampling of signals with finite rate of innovation," in *Proc. IEEE Int. Conf. Acoust., Speech, Signal Process.*, 2014, pp. 1803–1807.

[32] M. Unser and T. Blu, "Cardinal exponential splines: Part I-theory and filtering algorithms," *IEEE Trans. Signal Process.*, vol. 53, no. 4, pp. 1425–1438, Apr. 2005.

[33] A. Roy and E. Hendriks, "Van Gogh's "Sunflowers" in London and Amsterdam," *Nat. Gallery Tech. Bull.*, vol. 37, pp. 60–77, 2016.

[34] C. Higgitt *et al.*, "'Methods, materials and condition of the London Sunflowers' in Van Gogh's Sunflowers illuminated: Art meets science," *Van Gogh Museum Studies*, pp. 49–83, 2019.

[35] L. Keith *et al.*, "Leonardo da Vinci's "Virgin of the rocks": Treatment, technique and display," *Nat. Gallery Tech. Bull.*, vol. 32, pp. 32–56, 2011.
[36] M. Spring *et al.*, "Leonardo's Virgin of the rocks in the national gallery, London; New discoveries from macro X-Ray fluorescence scanning and reflectance imaging spectroscopy," *Nat. Gallery Tech. Bull.*, vol. 41, pp. 68–117, 2021.
[37] P. L. Dragotti, M. Vetterli, and T. Blu, "Sampling moments and reconstructing signals of finite rate of innovation: Shannon meets Strang–Fix," *IEEE Trans. Signal Process.*, vol. 55, no. 5, pp. 1741–1757, May 2007.
[38] P. Milanfar, G. C. Verghese, W. C. Karl, and A. S. Willsky, "Reconstructing polygons from moments with connections to array processing," *IEEE Trans. Signal Process.*, vol. 43, no. 2, pp. 432–443, Feb. 1995.
[39] B. Gustafsson *et al.*, "Reconstructing planar domains from their moments," *Inverse Problems*, vol. 16, no. 4, 2000, Art. no. 1053.
[40] M. Elad, P. Milanfar, and G. H. Golub, "Shape from moments-an estimation theory perspective," *IEEE Trans. Signal Process.*, vol. 52, no. 7, pp. 1814–1829, Jul. 2004.
[41] P. R. Bevington and D. K. Robinson, *Data Reduction and Error Analysis for the Physical Sciences*. New York, NY, USA: McGraw-Hill, 1992.
[42] A. Thompson *et al.*, "X-Ray data booklet (2009)," *Lawrence Berkeley National Laboratory*, Univ. California, Berkeley, CA, USA, 2009.

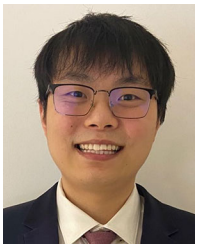

Su Yan (Student Member, IEEE) received the B.Eng. degree in communication engineering from Jilin University, Changchun, China, in 2016 and the M.Sc. degree in communication engineering with Distinction from The University of Manchester, Manchester, U.K., in 2017. He is currently working toward the Doctoral degree with Electrical and Electronic Engineering Department, Imperial College London, London, U.K., under the supervision of Professor Pier Luigi Gragotti. His research interests include applications of Finite Rate of Innovation (FRI) sampling theory, inverse problems, MA-XRF spectrum deconvolution, and MA-XRF super-resolution.

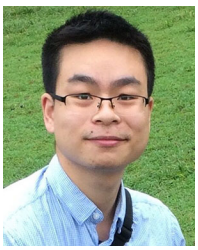

Jun-Jie Huang (Member, IEEE) received the B.Eng. (Hons.) degree (with First Class Honours) in electronic engineering and the M.Phil. degree in electronic and information engineering from The Hong Kong Polytechnic University, Hong Kong, China, in 2013 and 2015, respectively, and the Ph.D. degree from Imperial College London (ICL), London, U.K., in 2019. He is currently a Postdoc with Communications and Signal Processing (CSP) Group, Electrical and Electronic Engineering Department, ICL. His research interests include the areas of computer vision, signal processing and deep learning, specifically, for inverse problems, model-based deep learning, computational imaging.

Nathan Daly received the Ph.D. degree in chemistry from Columbia University, New York, NY, USA, in 2017 and is currently a Postdoctoral Research Fellow with the Scientific Department of the National Gallery funded by an EPSRC research grant with University College London and Imperial College London, London, U.K., titled Art through the ICT Lens (ARTICT): Big Data Processing Tools to Support the Technical Study, Preservation and Conservation of Old Master Paintings. In this role, he specializes in the acquisition of MA-XRF and hyperspectral data of both reference materials and paintings in the National Gallery collection and their subsequent preprocessing and analysis. Previously, he was a Postgraduate Fellow with Getty Conservation Institute focusing on non-invasive analysis of works on paper, particularly carbon-based black media, using Raman microspectroscopy, MA-XRF scanning, and hyperspectral imaging.

His research interests include the use of various non-invasive spectroscopic mapping and imaging techniques in the cultural heritage field, as well as multivariate statistical methods to better interrogate these datasets. He is particularly interested in developing methods to combine complementary datasets in order to improve their interpretation and the application of this information by museum conservators and curators.

Catherine Higgitt received the Ph.D. degree in chemistry from the University of York, York, U.K., and joined the National Gallery in 1999, as an Organic Analyst, specialising in the study of paint binding media and other organic natural product materials associated with paintings using a combination of spectroscopic and chromatographic techniques. She has a particular interest in the ageing, deterioration and interactions undergone by materials and the impact such interactions can have on the interpretation of analytical results.

Between 2007 and 2015, she was the Head of science at the British Museum, gaining experience working with a wider variety of materials and handling data acquired using a very broad range of analytical and imaging techniques including multispectral imaging techniques.

In 2015, she returned to the National Gallery, as a Principal Scientist, building on her previous research and helping extend the range of analytical and imaging approaches available for the study of paintings. Her role has included introducing the use of MA-XRF scanning into institutional practice and helping to develop cutting edge visible-nIR-SWIR hyperspectral imaging equipment for use at the NG. As the majority of methods she employs, whether on micro-samples (e.g. GC-MS, HPLC-PDA, ATR-FTIR, SEM-EDX) or in-situ on paintings (MA-XRF, OCT and HSI) generate 3D datasets or datacubes she is increasingly concerned with how best to interrogate, interpret and present this data and possibilities to combine datasets to enrich understanding. She has extensive experience in the application and publication of her research for different academic audiences, including both art-historical and scientific, and wider public.

Pier Luigi Dragotti (Fellow, IEEE) received the Laurea degree (summa cum laude) in electronic engineering from the University Federico II, Naples, Italy, in 1997, the master's degree in communications systems from the Swiss Federal Institute of Technology of Lausanne (EPFL), Switzerland, in 1998, and the Ph.D. degree from EPFL, Switzerland, in April 2002. He is currently a Professor of signal processing with Electrical and Electronic Engineering Department, Imperial College London, London, U.K. Before joining Imperial College in November 2002, he was a Senior Researcher with EPFL, working on distributed signal processing for Swiss National Competence Center in Research on Mobile Information and Communication Systems. He has also held several visiting positions. He was a Visiting Student with Stanford University, Stanford, CA, USA, in 1996, a Summer Researcher with the Mathematics of Communications Department, Bell Labs, Lucent Technologies, Murray Hill, NJ, USA, in 2000, and a Visiting Scientist with the Massachusetts Institute of Technology, Cambridge, MA, USA, in 2011. His research interests include sampling theory, wavelet theory and its applications, sparsity-driven signal processing, and computational imaging.

He was the Editor-in-Chief of the IEEE TRANSACTIONS ON SIGNAL PROCESSING during 2018–2020, a Member of the IEEE SPS Fellow Evaluation Committee during 2020–2021, an Associate Editor for the IEEE TRANSACTIONS ON IMAGE PROCESSING during 2006–2009, and an Elected Member of the IEEE Image, Video and Multidimensional Signal Processing Technical Committee during 2008–2013, where he acted as chair of the award sub-committee during 2011–2013. He was a Member of the IEEE Signal Processing Theory and Methods Technical Committee during 2013–2018. He was a Member of the Computational Imaging Technical Committee during 2015—2020. He was also the Technical Co-Chair for the European Signal Processing Conference (Eusipco) in 2012. Dragotti was also the recipient of the European Research Council (ERC) Investigator Award during 2011–2016. He is currently an IEEE SPS Distinguished Lecturer.